eNeuro

Research Article: New Research | Disorders of the Nervous System

Microglial Expression of the Wnt Signaling Modulator *DKK2* Differs between Human Alzheimer's Disease Brains and Mouse Neurodegeneration Models

https://doi.org/10.1523/ENEURO.0306-22.2022

Cite as: eNeuro 2023; 10.1523/ENEURO.0306-22.2022

Received: 25 July 2022
Revised: 12 December 2022
Accepted: 13 December 2022

Title: Microglial expression of the Wnt signalling modulator *DKK2* differs between human Alzheimer's disease brains and mouse neurodegeneration models

Abbreviated title: DKK2 levels differ in mouse/human AD microglia

Authors: Nozie D. Aghaizu [1,*], Sarah Jolly [2,*], Satinder K. Samra [1], Bernadett Kalmar [3], Katleen Craessaerts [5,6], Linda Greensmith [3], Patricia C. Salinas [4], Bart De Strooper [1,5,6], and Paul J. Whiting [1,2]

Author affiliations and footnotes:

[1] UK Dementia Research Institute at University College London, Cruciform Building, Gower Street, London WC1E 6BT, United Kingdom

[2] ARUK Drug Discovery Institute (DDI), University College London, Cruciform Building, Gower Street, London WC1E 6BT, United Kingdom

[3] Department of Neuromuscular Diseases, UCL Queen Square Motor Neuron Disease Centre, Queen Square Institute of Neurology, Queen Square, London WC1N 3BG, United Kingdom

[4] Department of Cell and Developmental Biology, University College London, Gower Street, London WC1E 6BT, United Kingdom

[5] VIB Centre for Brain Disease Research, Onderwijs en Navorsing 5, 3000, Leuven, Belgium

[6] KU Leuven, Department of Neurosciences and Leuven Brain Institute, Oude Markt 13 – bus 5005, 3000, Leuven, Belgium

* Correspondence: NDA, nozie.aghaizu@ucl.ac.uk, Tel.: +44 (0)20 3108 6890; SJ, sarah.jolly@ucl.ac.uk, Tel.: +44 (0)20 7679 52746

Author contributions: (CRediT taxonomy) Conceptualisation, N.D.A., S.J., and P.J.W.; Methodology, N.D.A., S.J., S.K.S., B.K., and K.C.; Software, N.D.A. and S.J.; Validation, N.D.A. and S.J.; Formal Analysis, N.D.A.; Investigation, N.D.A. and S.J.; Resources, L.G., P.C.S., B.D.S., and P.J.W.; Writing – Original Draft, N.D.A.; Writing – Review & Editing, N.D.A., S.J., L.G., P.C.S., B.D.S., and P.J.W.; Funding Acquisition, L.G., P.C.S., B.D.S., and P.J.W.; Supervision, P.J.W.

Number of pages: 74

Number of figures including extended figures: 11

Number of tables including extended tables: 3

Number of words: 2759 (abstract (250), significance statement (120), introduction (712), and discussion (1699))

Acknowledgements: We thank Dr. C.S. Frigerio for constructive discussions.

Conflict of interest statement: The authors declare no competing financial interests

Funding sources: This work was supported by the UK Dementia Research Institute, which receives its funding from DRI Ltd, funded by the UK Medical Research Council, Alzheimer's Society and Alzheimer's Research UK. LG and BK are supported by Brain Research UK and the Rosetrees Trust. We thank the Queen's Square Brain Bank for providing human samples.

Abstract: Wnt signalling is crucial for synapse and cognitive function. Indeed, deficient Wnt signalling is causally related to increased expression of *DKK1,* an endogenous negative Wnt regulator, and synapse loss, both of which likely contribute to cognitive decline in Alzheimer's disease (AD). Increasingly, AD research efforts have probed the neuroinflammatory role of microglia, the resident immune cells of the central nervous system (CNS), which have furthermore been shown to be modulated by Wnt signalling.

The *DKK1* homologue *DKK2* has been previously identified as an activated response and/or disease-associated microglia (DAM/ARM) gene in a mouse model of AD. Here we performed a detailed analysis of *DKK2* in mouse models of neurodegeneration, and in human AD brain. In *APP/PS1* and $APP^{NL\text{-}G\text{-}F}$ AD mouse model brains as well as in $SOD1^{G93A}$ ALS mouse model spinal cords, but not in control littermates, we demonstrated significant microgliosis and microglial *Dkk2* mRNA upregulation in a disease-stage dependent manner. In the AD models, these DAM/ARM $Dkk2^{+}$ microglia preferentially accumulated close to βAmyloid plaques. Furthermore, recombinant DKK2 treatment of rat hippocampal primary neurons blocked WNT7a-induced dendritic spine and synapse formation, indicative of an anti-synaptic effect similar to that of DKK1. In stark contrast, no such microglial *DKK2* upregulation was detected in the post-mortem human frontal cortex from individuals diagnosed with AD or pathological ageing.

In summary, the difference in microglial expression of the DAM/ARM gene *DKK2* between mouse models and human AD brain highlights the increasingly recognised limitations of using mouse models to recapitulate facets of human neurodegenerative disease.

Keywords: Alzheimer's disease, Neurodegeneration, Microglia, Neuroinflammation, Wnt signalling,

Significance statement: The endogenous negative Wnt regulator *Dkk2* is significantly upregulated at the mRNA level in microglia of AD mouse models, implying that microglia derived Dkk2 protein may detrimentally contribute to a reduced Wnt signalling tone in the AD brain, a known pathophysiological manifestation. Indeed, recombinant DKK2 prevented Wnt-dependent synapse formation in cultured neurons. However, *DKK2* upregulation was not recapitulated in post-mortem human AD brains.

The success of neurodegeneration animal models has relied on pathophysiology that for the most part correctly modelled human disease. Increasingly however, limitations to the validity of mouse models to recapitulate human neurodegenerative disease have become apparent, as evidenced by the present study by the difference in microglial *DKK2* expression between AD mouse models and human AD brain.

Introduction:

Microglia, the resident immune cells of the central nervous system (CNS), contribute both beneficially and detrimentally to Alzheimer's disease (AD) in a context-dependent manner, thus rendering their response to AD heterogeneous in nature. So too is their phenotype at the transcriptomic, proteomic, epigenomic, metabolomic, and morphological level leading to the identification of spatio-temporally distinct microglial subpopulations (reviewed by Masuda et al., 2020; Paolicelli et al., 2022). Disease associated (DAM) – or activated response microglia (ARM; henceforth: DAM/ARM) – represent a subpopulation associated with the neurodegenerative brain (Keren-Shaul et al., 2017; Sala Frigerio et al., 2019). Transitioning from homeostatic to DAM/ARM-state requires TREM2 (triggering receptor expressed on myeloid cells-2) (Keren-Shaul et al., 2017). A bona fide receptor for βAmyloid, TREM2 ligation activates microglia and orchestrates a gene regulatory response that increases inflammatory signalling, phagocytosis, and proliferation, a response thought to restrict development of AD (reviewed in Gratuze et al., 2018).

TREM2 regulates microglial proliferation and survival by activating, among others, the canonical Wnt/β-catenin pathway (Zheng et al., 2017; reviewed in Aghaizu et al., 2020). Indeed, several genes upregulated by TREM2 in response to AD pathology are related to proliferation and Wnt signalling (Meilandt et al., 2020). The canonical Wnt signalling modulatory gene *Dkk2* (Mao and Niehrs, 2003) was upregulated downstream of *Trem2* in DAM/ARM cells in *APP/PS1*, *PS2APP, 5xFAD, and* $APP^{NL\text{-}G\text{-}F}$ AD mouse models in separate studies, making it a putative DAM/ARM marker gene (Friedman et al., 2018; Sala Frigerio et al., 2019; Meilandt et al., 2020). Database searches further indicate that while control CNS *DKK2/Dkk2* expression levels are generally low across the various cell types, they are respectively either similar or greater in non-microglial CNS cell populations compared with microglia in human and mouse single cell RNA-Seq studies (Zhang et al., 2014, 2016; Friedman et al., 2018). The secreted protein DKK2 belongs to the Dickkopf family of Wnt modulators (Niehrs, 2006). Its homologue DKK1 antagonises Wnt signalling through Frizzled

Wnt receptors by sequestering the co-receptor LRP5/6 (Bafico et al., 2001; Mao et al., 2001). The reduced Wnt signalling tone evident in AD is at least partially due to Aβ fibril-induced upregulation of *DKK1/Dkk1* in human AD and AD mouse models (Caricasole et al., 2004; Rosi et al., 2010; Killick et al., 2014; Sellers et al., 2018; Jackson et al., 2019). This was synaptotoxic in *in vitro* and *in vivo* models (Purro et al., 2012; Galli et al., 2014; Marzo et al., 2016; Elliott et al., 2018; Sellers et al., 2018), and potentially also in human AD (Jackson et al., 2019).

Much less is known about the role of microglial *DKK2* in the CNS, not to mention in AD. In cell lines, DKK2 can both antagonise and agonise Wnt-LRP6 signalling depending respectively on the presence or absence of the second co-receptor Kremen2 (Mao and Niehrs, 2003). During neural crest specification, DKK2 agonises Wnt signalling (Devotta et al., 2018). Conversely, in cancer studies DKK2 generally inhibits Wnt signalling (Kuphal et al., 2006; Sato et al., 2007; Maehata et al., 2008; Hirata et al., 2009; Zhu et al., 2012; Mu et al., 2017). Furthermore, cancer cell-secreted DKK2 suppresses immune cell activation via an unconventional Wnt-unrelated pathway (Xiao et al., 2018). In the aforementioned single-cell and bulk cell gene expression studies on neurodegeneration mouse models, *Dkk2* was upregulated in microglia, but no information on the spatial relationship between *Dkk2*$^{+}$ microglia and neurodegenerative pathology or the biological role of this upregulation was provided (Friedman et al., 2018; Sala Frigerio et al., 2019; Meilandt et al., 2020). To address this gap in our knowledge, we performed a histological assessment of microglial *Dkk2/DKK2* upregulation in several mouse models and in human AD, and furthermore investigated the effect of recombinant DKK2 on cultured primary neurons.

Here, we report significant microgliosis and microglial *Dkk2* mRNA upregulation in a disease-stage dependent manner in *APP/PS1,* and *APP*$^{NL\text{-}G\text{-}F}$ AD mouse model brains. Clustering of *Dkk2*$^{+}$ microglia around amyloid plaques was often more pronounced than that of *Dkk2*$^{-}$ microglia. In cultured rat neurons, recombinant DKK2 blocked Wnt dependent synapse formation. Crucially however, microglial *DKK2* upregulation was not detected in

post-mortem human brain from individuals diagnosed with AD or pathological ageing. This non-universality of what was a putative DAM/ARM marker gene highlights the increasingly recognised limitations of using animal models to recapitulate facets of human neurodegenerative disease.

Materials and Methods:

Mice

Mouse CNS tissue was obtained from the following sources: Brain tissue from male and female *B6.Cg-Tg*(*APPswe, PSEN1dE9*) mice (Jankowsky et al., 2004; RRID:MMRRC_034829-JAX; abbreviated: *APP/PS1*) and age-matched wild-type *C57BL/6J* control mice at 3, 8, and 12 months was purchased from WuXi AppTec. Brain tissue from male homozygous *B6.129S5-Apptm3.1Tcs* mice (Saito et al., 2014; RRID:IMSR_RBRC0634; backcrossed for at least 2 generations with *C57BL/6J* mice; here referred to as $APP^{NL\text{-}G\text{-}F}$) and age-matched wild-type *C57BL/6J* control mice at 7 and 24 months was kindly provided by the De Strooper lab. Spinal cord tissue from female mice expressing mutant human $SOD1^{G93A}$ (*B6SJL-Tg[*$SOD1^{G93A}$*]1Gur/J*; Gurney et al., 1994; RRID:IMSR_JAX:002726; abbreviated: $SOD1^{G93A}$) and age-matched female control mice expressing wild-type human *SOD1* (*B6SJLTg[SOD1]2Gur/J*; Gurney et al., 1994; RRID:IMSR_JAX:002297; abbreviated: $SOD1^{WT}$) at 50, 100, and 120 days was kindly provided by the Greensmith lab. Colonies were maintained by breeding male heterozygous carriers with female (*C57BL/6* × *SJL*) F1 hybrids. Mice were genotyped for the human *SOD1* transgene from ear or tail genomic DNA.

In every case, mice were housed according to the appropriate institution's ethical requirements, and in compliance to the country's laws for animal research. Typically, mice were housed in standard individually ventilated cages with ≤ 3 mice per cage at 21 ± 1 °C with relative humidity 55 ± 10 % and maintained on a 12-hour light/dark cycle with access to food (standard pellets), water, and nesting material provided *ad libitum* via an overhead rack. At the onset of pathology, affected animals were provided with food pellets soaked in water at ground level to ensure sufficient nourishment and hydration. Cages were checked daily to ensure animal welfare. Body weight was assessed regularly to ensure no weight loss. For animals housed at WuXi AppTec, studies were reviewed and approved by Institutional Animal Care and Use Committee (IACUC) of WuXi AppTec (Suzhou) Co., Ltd. For animals

housed at VIB/KU Leuven, studies were approved by the KU Leuven Ethical Committee and in accordance with European Directive 2010/63/EU. For animals housed at UCL, studies were carried out following the guidelines of the UCL Institute of Neurology Genetic Manipulation and Ethic Committees and in accordance with the European Community Council Directive of November 24, 1986 (86/609/EEC). Animal experiments were undertaken under licence from the UK Home Office in accordance with the Animals (Scientific Procedures) Act 1986 (Amended Regulations 2012) and were approved by the Ethical Review Panel of the Institute of Neurology.

For tissue collection, animals were injected with terminal anaesthesia (pentobarbital sodium, Euthatal) and were transcardially perfused with PBS by trained personnel.

Rats

Animal experiments were undertaken under licence from the UK Home Office in accordance with the Animals (Scientific Procedures) Act 1986 (Amended Regulations 2012) and in compliance with the ethical standards at University College London (UCL). Timed matings were set up for Sprague-Dawley rats (RRID:MGI:5651135) for subsequent harvesting of embryos at embryonic day (E)18. Pregnant rat dams were sacrificed using Isoflurane and cervical dislocation.

Human post-mortem tissue

Anonymised human samples from control, pathological ageing, and AD subjects were obtained from the Queen's Square Brain Bank for Neurological Disorders (QSBB) and NeuroResource, UCL Institute of Neurology, University College London. All samples were obtained with informed consent in accordance with the Human Tissue Act 2004 and under the UCL Institute of Neurology HTA material transfer agreement UCLMTA1/17 approved by

the NHS Research Ethics Committee. Post-mortem frontal cortex biopsy tissue was harvested, snap-frozen, and stored at -80 °C until further tissue processing. All experiments were performed in accordance with relevant guidelines and regulations. Sample information including demographic data, disease classifications and post-mortem intervals is shown in Table 6-1.

Tissue processing

Mouse brain tissue, freshly harvested upon transcardial perfusion with PBS, was post-fixed by immersion in 4 % paraformaldehyde (PFA) in PBS overnight at 4 °C followed by overnight immersion in and equilibration to 20 % sucrose in PBS at 4 °C. Mouse brains were split into 3 segments by applying 2 equidistant coronal slice cuts along the rostro-caudal axis, resulting in an olfactory bulb containing rostral-most segment, a hippocampus containing middle segment and the caudal-most cerebellar segment. After embedding in OCT (CellPath) and freezing in 2-methylbutane (Sigma) pre-chilled in liquid Nitrogen, the middle segment was coronally cryosectioned at 15 µm thickness on a Leica CM1860UV cryostat (Leica) and sections containing clearly defined hippocampus were transferred onto Superfrost Plus Gold microscopy slides (ThermoScientific).

Mouse spinal cord tissue was processed identically but split only into 2 segments by applying a transverse slice cut rostral to the lumbar enlargement, resulting in a rostral cervical/thoracic segment and a caudal lumbar segment. The cryo-embedded lumbar segment was transversally cryosectioned at 15 µm thickness and sections containing clearly defined L5 lumbar spinal cord were transferred onto Superfrost Plus Gold microscopy slides (ThermoScientific).

Human frontal cortex brain tissue was cryosectioned at 15 µm thickness, sections were transferred onto Superfrost Plus Gold microscopy slides (ThermoScientific) and dried for 10 min at 40 °C.

Human and mouse sections were stored at -80 °C until staining.

mRNA fluorescence *in situ* hybridisation (FISH)

mRNA fluorescence *in situ* hybridisation for mouse *Dkk2* and human *DKK2*, *TREM2*, and *P2RY12* mRNA was performed on mouse brain / spinal cord and human frontal cortex cryosections respectively, by using the Multiplex Fluorescent V2 Assay Kit (ACD Bio).

Briefly, mouse cryosections were thawed and dried at 40 °C for 4 min prior to post-fixation with 4 % PFA in PBS at room temperature (RT) for 10 min. OCT residue was washed off by applying 1 x PBS for 5 min at RT. Sections were treated with RNAScope H_2O_2 for 4 min at RT and subsequently washed 2 x 3 min with UltraPure Distilled Water (Invitrogen) at RT. Microscopy slides containing cryosections were submerged for 4 min in boiling 1 x RNAScope target retrieval solution followed by immediate submersion in UltraPure Distilled Water. Cryosections were dehydrated in 100 % ethanol at RT for 2 min and allowed to air dry at RT for 5 min. Cryosections were subsequently treated with RNAScope Protease IV at RT for 15 min and washed 2 x 3 min at RT with 1 x PBS. RNAScope probes were allowed to hybridise to cryosections for 2 hrs at 40 °C (*Mm-Dkk2*-C1, 404841; *Mm-Ppib*-C1 (positive control probe), 313911; *E. coli-Dapb*-C1 (negative control probe), 310043). Probes were detected with TSA-Cy3 (Perkin Elmer, FP1170) using the RNAScope branched DNA amplification principle as per the manufacturer's instructions. Subsequently, cryosections were further immunohistochemically processed (see below).

Human cryosections were processed similarly as previously described (Jolly et al., 2019). Briefly, cryosections were thawed and dried at 40 °C for 4 min prior to post-fixation with chilled 4 % PFA in PBS at 4 °C for 30 min followed by 2 x 2 min washes with 1 x PBS at RT. Cryosections were then dehydrated in an ethanol dilution series (50 %, 70 %, 2 x 100 %) at RT for 5 min each and subsequently allowed to air dry at RT for 5 min. Sections were treated with RNAScope H_2O_2 for 10 min at RT and subsequently washed 2 x 2 min with 1 x PBS.

Microscopy slides containing cryosections were submerged for 10 min in boiling 1 x RNAScope target retrieval solution followed by 2 x 2 min washes with 1 x PBS. Cryosections were subsequently treated with RNAScope Protease IV at RT for 20 min and washed 2 x 3 min at RT with 1 x PBS. RNAScope probes were allowed to hybridise to cryosections for 2 hrs at 40 °C (*Hs-TREM2*-C1, 420491; *Hs-DKK2*-C2, 531131-C2; *Hs-P2RY12*-C3; 450391-C3; *Hs-PPIB*-C1 (positive control probe), 313901; *E. coli-Dapb*-C1 (negative control probe), 310043). C2 and C3 probes were diluted in C1 probe solution at a 1:50 ratio. Probes were detected with TSA-Cy3 (Perkin Elmer, FP1170), Opal 620 (Akoya, FP1495001KT), and TSA-Cy5 (Perkin Elmer, REF FP1168) using the RNAScope branched DNA amplification principle as per the manufacturer's instructions. Subsequently, cryosections were further immunohistochemically processed (see below).

Primary hippocampal neuron cultures

Primary rat hippocampal neuron cultures were prepared from embryonic day 18 (E18) Sprague-Dawley rat embryos. One day prior to neuron isolation, 8 well chamber slide dishes (Miltenyi Biotec) were coated over night with 1 mg/ml poly-L-lysine in borate buffer (boric acid, 3.1 g/l; borax 4.8 g/l; pH 8.5). On the day of the neuron isolation, dishes were washed 3 x 20 min with UltraPure Distilled Water, filled with plating medium (Neurobasal (ThermoFisher) supplemented with 1x B27 (ThermoFisher), 1x GlutaMAX (ThermoFisher), 1x Penicillin-Streptomycin (ThermoFisher), 25 µM L-glutamate (Sigma)), and pre-equilibrated at 5 % CO_2, 37 °C. Hippocampi were dissected from brain tissue using sterilized tools (Dumont #5 fine tip tweezers, Dumont #7 curved forceps, Student Vannas Scissors 9cm long/straight; Fisherbrand) and collected in ice cold HBSS (Invitrogen). Following three washes with fresh ice cold HBSS, hippocampi were enzymatically dissociated by incubation in accutase (ThermoFisher) at 37 °C for 10 min, providing manual agitation every 2-3 min. Hippocampi were then washed three times with pre-warmed (37 °C) HBSS, followed by mechanical dissociation into a single cell suspension by trituration in

HBSS using a 1 mL pipette. Live cell density was determined using the Countess 3 automated cell counter (ThermoFisher) and cells were plated onto 8 well chamber slides at a density of 43,000 cells/cm^2 and cultured in an incubator at 37 °C / 5 % CO_2. Half medium changes were performed twice per week with maintenance medium: Neurobasal, supplemented with 1x B27, 1x GlutaMAX, 1x Penicillin-Streptomycin.

Neuronal transfection with the DNA construct *pHR hsyn:EGFP* (Keaveney et al., 2018; kind gift from Xue Han (Addgene plasmid # 114215; http://n2t.net/addgene:114215; RRID:Addgene_114215)) was performed at 7 days *in vitro* (DIV) using the Neuromag magnetofection method (OzBiosciences). Briefly, for every 40,000 cells plated per well of an 8 well chamber slide dish, 0.5 µg DNA was mixed and complexed with 1 µl Neuromag transfection reagent in 100 µl of OptiMem (all reagents at room temperature). Following 20 min incubation at room temperature, the transfection mix was added dropwise to neuronal cultures and the culture dish was placed on a magnetic plate (OzBiosciences) pre-equilibrated to 37 °C inside an incubator for the magnetofection step. After 20 min of magnetofection in the incubator, cell culture dish was removed from the magnetic plate and normal cell culture resumed.

Recombinant protein treatment was performed at 21 DIV for 24 hours: human DKK2 (Bio-Techne, 6628-DK-010/CF, 100 ng/ml), human DKK1 (Bio-Techne, 5439-DK-010/CF, 100 ng/ml), human WNT7a (Bio-Techne, 3008-WN-010/CF, 200 ng/ml); 100 ng/ml bovine serum albumin (BSA) in 1x PBS heat inactivated at 95 °C for 5 min was used as control.

Fixation was performed following 24 hrs of recombinant protein treatment using 4 % PFA / 4 % Sucrose (Sigma) in 1x PBS at RT for 15 min. Neurons were subsequently washed 3 x with 1x PBS.

Immunocytochemistry and immunohistochemistry

Tissue sections stained by mRNA FISH and fixed primary neurons were washed with 1 x PBS and blocked in 1 x PBS supplemented with 5 % (vol/vol) goat serum (Bio-Rad), 1 % (wt/vol) BSA (Sigma) and 0.1 % (vol/vol) Triton X-100 (Sigma) at RT for 1h. Primary antibodies were diluted in blocking solution and applied to samples at 4 °C overnight. Primary antibodies used in this study were: βAmyloid (BioLegend, 803001, RRID: AB_2564653, 1:200), GFAP (Sigma, G3893, RRID:AB_477010, 1:500), Homer (SynapticSystems, 160003, RRID:AB_887730, 1:500), Iba1 (Fujifilm Wako, 019-19741, RRID:AB_839504, 1:250), misfolded SOD1 (Médimabs, MM-0070-P, RRID:AB_10015296, 1:100), vGlut (MerckMillipore, AB5905, RRID:AB_2301751, 1:300); negative controls omitted the primary antibody. This was followed by 4 x 10 min washes in 1 x PBS at RT and subsequent application of suitable goat Alexa Fluor Plus secondary antibodies (488/546/647) diluted 1:500 in blocking solution at RT for 2 hrs. Samples were then washed 4 x 10 min with 1 x PBS at RT. Cryosections only were treated with 1x TrueBlack (Biotium) at RT for 30 sec to quench autofluorescence caused by the accumulation of lipofuscin and other protein aggregates, followed by 2 x washes with 1 x PBS. Nuclei of samples were counterstained with DAPI (Sigma; shown in blue in all confocal images) at 1 µg/ml in PBS and samples were mounted using DAKO Fluorescence Mounting Medium (Agilent).

Microscopy

Stained tissue was imaged using a Zeiss LSM 880 confocal laser scanning microscope fitted with 40x (NA = 1.3) and 63x (NA = 1.4) objectives and photomultiplier tubes to detect fluorescence emission. For image acquisition, *xyz* confocal stacks were captured at a resolution of 1024 x 1024 pixels and at a step size of 1 µm. Microscope settings were established during first acquisition and subsequently not further modified. Four distinct fields of view were imaged from two representative sections per sample.

For image acquisition of transfected primary rat hippocampal neurons following recombinant protein treatment, whole neurons were acquired using the 40x objective and secondary dendrites were acquired with higher magnification using the 63x objective with an additional 3.5x zoom at a resolution of 1024 x 1024 pixels and at a step size of 0.5 µm. A total of 15 neurons and accompanying secondary dendrites spread across three biological repeats were imaged per condition.

Image processing and analysis

All images acquired from mouse tissue were processed and analysed in Fiji/ImageJ (Schindelin et al., 2012). *xyz* confocal stacks were collapsed into maximum *z* projections. Microgliosis was assessed by measuring both the number of microglia ($DAPI^+$ nuclei embedded within typical microglial Iba1 immunoreactivity) and the total 2D surface area of Iba1 immunoreactivity within the acquired field of view. For area quantification, Iba1 immunoreactivity was processed by applying the 'Remove Outliers' function to remove non-specific noise (bright, radius = 2, threshold = 50), followed by thresholding at 35/255 to define the signal range, and two further rounds of the 'Remove Outliers' function, to fill-in nuclear and other gaps in Iba1 staining (dark, radius = 1), and to further remove non-specific noise (bright, radius = 3). The created Iba1 surface area was measured and used as a mask within which the *Dkk2* mRNA FISH signal surface area, thresholded to 30/255, was quantified. Normalised *Dkk2* area per microglial cell was determined by dividing the total measured *Dkk2* area by the number of detected $Iba1^+/DAPI^+$ microglia within a given field of view.

Human frontal cortex image acquisitions were first subjected to 'Linear unmixing' with automatic fluorophore detection within the Zeiss Zen Black software (Zeiss) to remove overlapping signals between the five fluorophore channels. Unmixed and maximum z

projected images were subsequently processed and analysed using the HALO FISH-IF v2.0.4 module (Indica Labs). The *DKK2* mRNA FISH signal surface area associated with *TREM2/P2RY12* double positive microglia cells was quantified. To achieve this, cell nuclei and their *xy* coordinates were recorded based on DAPI signal. Probe detection was optimised based on signal size, intensity of positive probe pixels and contrast threshold parameter settings (see Table 6-2). The maximum distance threshold for probe signal assignment to nuclei was 25 µm. We classified cells positive for *P2RY12* and *TREM2* as microglia (DAPI^{+}/*P2RY12/TREM2*$^{+}$), determined their number, and measured the surface area of *DKK2* mRNA FISH signal associated with such DAPI^{+}/*P2RY12/TREM2*$^{+}$ cells. Normalised *DKK2* area per microglial cell was determined by dividing the total measured *DKK2* area by the number of detected DAPI^{+}/*P2RY12/TREM2*$^{+}$microglia within a given field of view.

Microglia-βAmyolid plaque distance analysis: we determined the 2D Euclidian distance of microglia to the proximal most βAmyolid plaque dense core in maximum projected images according to the following Fiji/ImageJ methodology: an intensity threshold was applied to the image channel containing βAmyloid immunostaining to identify the plaque dense core, which was usually more intensely labelled compared with the plaque periphery; due to the heterogeneous nature of βAmyloid plaques, threshold values were determined for each acquired image. In early-stage *APP/PS1,* and *APP*$^{NL\text{-}G\text{-}F}$ AD mouse or littermate control tissue devoid of βAmyolid plaques, plaque dense core “placeholders” were randomly placed on confocal images by digitally drawing appropriately dimensioned white ellipses on the colour channel assigned to βAmyloid immunostaining using Fiji/ImageJ, followed by intensity threshold application as above. The binary dense core image generated in the previous step was subjected to the ‘Exact Signed Euclidian Distance Transform (3D)’ (EDT) plug-in to create a 2D map where distance to the closest dense core was encoded in grey values from -1024 (furthest possible distance) to 0 (at dense core edge). *xy* position landmarks of DAPI^{+}

387 microglia nuclear centres were placed on a binary image, which in turn was redirected to the
388 EDT image in the 'Set Measurements' window, selecting 'Mean grey value' as measurement
389 output. Note that *xy* positions of human microglia exported from HALO FISH-IF v2.0.4
390 module were imported into Fiji/ImageJ using the macro 'ImportXYcoordinates.ijm'. Grey
391 values at microglial *xy* positions were obtained using the 'Analyze Particles' function and
392 converted into distance units by multiplying the grey value by the image *xy* pixel dimension
393 (0.13495 µm) to yield microglia-βAmyloid plaque distances.

394

395 Dendritic spine and synapse analysis on *hSyn:EGFP* expressing primary rat hippocampal
396 neurons following recombinant protein treatment was performed using IMARIS software.
397 Briefly, the 'Filament' tool was used to semi-automatically specify the secondary dendrite
398 within an image file, followed by the detection of dendritic spines by manual identification.
399 Post-synaptic Homer immunoreactivity usually manifested as puncta in dendrites, especially
400 within dendritic spines. To quantify the number of Homer puncta exclusively within the
401 transfected secondary dendrite of interest, the GFP signal was used to create an exclusion
402 mask using the 'Surface' tool to isolate the Homer signal within the transfected dendrite.
403 Homer puncta were subsequently identified using the 'Spot' detection tool set to a detection
404 diameter of 0.45 µm; background Homer signal was excluded by thresholding using the
405 'Quality' filter. Pre-synaptic vGlut puncta in the entire image were similarly identified using
406 the 'Spot' detection tool at 0.45 µm diameter. Synapses were assumed using the 'Colocalize
407 spots' function within the 'Spot' detection tool when there was a maximum distance of 1 µm
408 between Homer and vGlut puncta.

409

410 Experimental design and statistical analysis

411 All means are stated ± standard deviation (SD). For the histological study aspects, *N* =
412 number of subjects (humans or animals) and *n* = number of fields of view. For qualitative

and quantitative histological assessments, we typically examined at least 4 subjects per group, imaging at least 4 different fields of view from 2 cryosections per subject, which met previously conducted sample size calculations according to Rosner (2015) with data inputs from Friedman et al., (2018). For the cytological study aspects, *N* = number of biological repeats, *n* = number of technical repeats (cells analysed). We used GraphPad Prism® software (GraphPad Software Inc.) for statistical analyses. D'Agostino and Pearson test was used to assess the normality of datasets. For the comparison of one independent variable between >2 groups, we used One-Way ANOVA with Tukey's multiple comparison test. For statistical tests involving two independent variables we used Two-Way ANOVA with Šidák multiple comparisons test; where data points were missing, Mixed-effects analysis with Šidák multiple comparisons test was utilised. Significance was accepted at $p \leq 0.05$ (see Table 1; alphabetical superscripts in results section and figure legends refer to Table 1).

Data, software, and code availability

The data sets generated during and/or analysed during the current study are available from the corresponding authors on request. The Fiji/ImageJ macro 'ImportXYcoordinates.ijm' is available on the Github repository available via https://github.com/DominicAghaizu/ImageJMacros/blob/main/ImportXYcoordinates.ijm.

436 **Results**

437 **Microgliosis and microglial *Dkk2* upregulation in *APP*$^{NL-G-F}$ mice**

438 We first investigated the microglial *Dkk2* expression pattern in the *APP*$^{NL-G-F}$ knock-in AD
439 mouse model, which develops robust pathology from the physiological expression of
440 humanised mouse amyloid precursor protein (*App*) harbouring Swedish, Beyreuther/Iberian,
441 and Arctic mutations (Saito et al., 2014). To this end, we performed mRNA FISH on coronal
442 brain cryosections to detect *Dkk2* mRNA *in situ* and acquired images from the motor cortex
443 and the *stratum pyramidale*, with adjacent *stratum oriens* and *stratum radiatum*, of the
444 hippocampal CA1 region, which are brain regions burdened by βAmyloid plaques,
445 neurofibrillary tangles and neuronal degeneration in AD patients and animal models. This
446 was paired with immunohistochemical labelling using antibodies against Iba1 and βAmyloid
447 to assess microglial *Dkk2* expression, as suggested previously (Friedman et al., 2018; Sala
448 Frigerio et al., 2019; Meilandt et al., 2020), and to evaluate the spatial relationship between
449 microglia and βAmyloid plaque lesions.

450 As expected, the brains of wild-type control littermate mice at 7 or 24 months were devoid of
451 βAmyloid plaques and exhibited normally tiled Iba1$^+$ microglia (Fig. 1*A,B*). In stark contrast,
452 we detected βAmyloid plaques in the cortex and CA1 of age-matched transgenic *APP*$^{NL-G-F}$
453 mice at 7 and 24 months (Fig. 1*A,B*). This was accompanied by robust microgliosis as
454 assessed by both normalised microglia cell count (DAPI$^+$/Iba1$^+$ cells) and area of Iba1 signal
455 in maximum *z*-projected image stacks (Fig. 1*C;* note that the microglia spatial distribution will
456 be addressed below). In the cortex, the number of microglia was significantly higher in
457 *APP*$^{NL-G-F}$ mice relative to age-matched littermate controls at 7 months (6.5 ± 0.8 vs. 3.0 ±
458 0.2 microglia per field of view (FOV; equal to 1.8 x 10^{-2} mm^2)) and at 24 months (15.9 ± 3.8
459 vs. 2.8 ± 0.8 to); significant differences were found between timepoints and genotypes (Fig.
460 1*A,D,G*; Two-Way ANOVA, p = 0.0101 and p = 0.0002 respectively [a]). Iba1 area was also
461 significantly elevated in transgenic mice compared with littermate controls, both at 7 months
462 (1505.8 ± 135.0 vs. 821.9 ± 239.3 μm^2) and 24 months (1982.4 ± 471.6 vs. 781.7 ± 121.1

μm^2) (Fig. 1*A*,*E*; Two-Way ANOVA, p = 0.1821 (timepoints) and p = 0.0018 (genotypes) [b]). To assess microglial *Dkk2* expression levels, we quantified *Dkk2* mRNA FISH signal that was colocalised with Iba1 immunoreactivity (Fig. 1*C*). The normalised area of *Dkk2* signal per DAPI$^+$/Iba1$^+$ microglial cell reached significantly higher levels in *APP$^{NL\text{-}G\text{-}F}$* mice relative to littermate controls, both at 7 months (0.3 ± 0.2 vs. 0.1 ± 0.1 μm^2) and at 24 months (1.2 ± 0.4 vs. 0.1 ± 0.1 μm^2) (Fig. 1*A*,*F*,*G*; Two-Way ANOVA, p = 0.0245 (timepoints) and p = 0.0013 (genotypes) [c]).

Similar patterns of microgliosis and *Dkk2* upregulation were observed in the hippocampal CA1 region. Microglia count numbers were markedly elevated in *APP$^{NL\text{-}G\text{-}F}$* mice compared with littermate controls both at 7 months (3.0 ± 1.1 vs. 2.6 ± 0.4 (n.s.)) and at 24 months (10.4 ± 2.3 vs. 2.7 ± 0.5) (Fig. 1*B*,*H*,*K*; Mixed-effects analysis, p = 0.0005 (timepoints) and p = 0.0051 (genotypes) [d]). Accordingly, detected Iba1 area was also increased: 1072.6 ± 146.3 vs. 846.9 ± 292.8 to μm^2 at 7 months and 1997.7 ± 511.8 vs. 970.6 ± 221.3 to μm^2 at 24 months (Fig. 1*B*,*I*; Two-Way ANOVA, p = 0.0119 (timepoints) and p = 0.0288 (genotypes) [e]). *Dkk2* expression per microglial cell quantified by mRNA FISH remained unchanged between *APP$^{NL\text{-}G\text{-}F}$* mice and littermate controls at 7 months (0.2 ± 0.1 vs. 0.2 ± 0.1 μm^2) but was higher at 24 months (0.6 ± 0.4 vs. 0.1 ± 0.0 μm^2) (Fig. 1*B*,*J*,*K*; Two-Way ANOVA, p = 0.1363 (timepoints) and p = 0.0652 (genotypes) [f]).

Finally, we also assessed whether there were genotype-related changes in the relative contribution of *Dkk2*$^+$ microglia versus the total microglia population. In the cortex, the percentage of *Dkk2*$^+$ microglia was significantly elevated in *APP$^{NL\text{-}G\text{-}F}$* mice compared with littermate controls both at 7 months (48.1 ± 22.3 vs. 18.8 ± 5.1 %) and at 24 months (84.1 ± 5.1 vs. 15.6 ± 7.7 %) (Fig. 1-1*A*; Two-Way ANOVA, p = 0.0240 (timepoints) and p = 0.0004 (genotypes) [g]). In the CA1 hippocampus, the percentage of *Dkk2*$^+$ microglia was similarly elevated in *APP$^{NL\text{-}G\text{-}F}$* mice compared with littermate controls at 7 months (34.9 ± 16.9 vs. 7.8 ± 9.4 %) and at 24 months (58.4 ± 21.6 vs. 18.4 ± 17.7 %) (Fig. 1-1*B*; Two-Way ANOVA, p = 0.0784 (timepoints) and p = 0.0093 (genotypes) [h]).

Taken together, our data demonstrate robust microgliosis in conjunction with *Dkk2* upregulation in $APP^{NL\text{-}G\text{-}F}$ mice compared with littermate controls, adding a spatial dimension to a previously published single-cell RNA sequencing (RNA-Seq) study that identified *Dkk2* expression in DAM/ARM microglia of the same mouse model (Sala Frigerio et al., 2019).

Microgliosis and microglial *Dkk2* upregulation in *APP/PS1* mice

Following investigation of $APP^{NL\text{-}G\text{-}F}$ mice, we assessed microgliosis and *Dkk2* upregulation in a second AD mouse model, the *APP/PS1* mouse, that expresses chimeric mutant mouse/human *App* and mutant human *presenilin 1*, both associated with early onset familial AD in humans (Jankowsky et al., 2004).

βAmyloid plaque load progressively increased in *APP/PS1* mice starting from 8 months, whereas age-matched wild-type control littermates lacked βAmyloid plaques altogether. This was especially evident in the cortex (Fig. 2*A*). While plaques were detectable in the hippocampus of *APP/PS1* mice (data not shown), CA1 *stratum pyramidale* proximal regions – the standardised hippocampal brain region that was imaged in our study – rarely exhibited plaque depositions (Fig. 2*B*).

While the number of $DAPI^+/Iba1^+$ microglia remained unchanged in *APP/PS1* mice versus littermate controls at 3 months (3.5 ± 0.6 to 3.3 ± 1.1 per FOV), their counts were significantly higher in *APP/PS1* relative to control mice at 8 months (6.1 ± 1.5 vs. 2.9 ± 0.5) and at 12 months (10.8 ± 1.5 vs. 3.0 ± 0.5 to) (Fig. 2*A*,*C*; Two-Way ANOVA, $p < 0.0001$ (timepoints) and $p < 0.0001$ (genotypes) [i]). Iba1 area did not markedly differ between transgenic and littermate control mice at 3 months (774.8 ± 175.2 vs. 935.4 ± 164.0 μm^2) and at 8 months (945.1 ± 275.8 vs. 764.1 ± 205.3 μm^2) but was significantly elevated in *APP/PS1* mice at 12 months (1811.1 ± 367.9 vs. 937.9 ± 220.8 μm^2) (Fig. 2*A*,*D*; Two-Way ANOVA, $p = 0.0030$ (timepoints) and $p = 0.0006$ (genotypes) [j]). Microgliosis in *APP/PS1* mice was accompanied by progressively increasing *Dkk2* expression per microglial cell at the mRNA level (1.2 ± 0.9 μm^2, 3.6 ± 2.5 μm^2, and 9.7 ± 5.5 μm^2 at 3/8/12 months), whereas this metric remained unchanged in age-matched littermate controls (0.9 ± 0.6 μm^2, 1.0 ± 0.7 μm^2 and 1.8 ± 1.2 μm^2) (Fig. 2*A*,*E*; Two-Way ANOVA, $p = 0.0003$ (timepoints) and $p = 0.0391$ (genotypes) [k]). The rate of increase of microgliosis (number of microglia) and *Dkk2* expression in *APP/PS1* mice was rapid between the ages of 3 and 8 months (88.3 ± 46.9 % for microgliosis, 208.6 ± 192.9 5 for *Dkk2* expression), at which point it plateaued (76.3 ±

24.6 % for microgliosis, 167.9 ± 138.2 % for *Dkk2* expression) (Fig. 2*A,F*). In agreement with published literature (Wang et al., 2003), we further noted that for the quantified metrics described above, female *APP/PS1* mice usually exhibited a more severe phenotype, especially at the final 12 months time point (Fig. 2*C,D,E*).

As noted above, hippocampal CA1 *stratum pyramidale* proximal regions in *APP/PS1* mice were mostly devoid of βAmyloid plaques. Here, we were unable to detect any changes in the number of $DAPI^+/Iba1^+$ microglia (Fig. 2*B,G,J*), Iba1 area (Fig. 2*B,H*), and *Dkk2* mRNA signal per microglial cell compared with age-matched littermate controls (Fig. 2*B,I,J*) (Two-Way ANOVA, all n.s.).

Finally, unlike in $APP^{NL\text{-}G\text{-}F}$ mice, we could not detect any significant timepoint-related changes in the relative contribution of $Dkk2^+$ microglia versus the total microglia population in *APP/PS1* mice compared with littermate controls both in the cortex (Fig. 2-1*A*; Two-Way ANOVA, p = 0.3563 (timepoints) and p = 0.7931 (genotypes) [l]) and in the CA1 hippocampus (Fig. 2-1*B*; Two-Way ANOVA, p = 0.1691 (timepoints) and p = 0.7041 (genotypes) [m]).

Thus, we were able to largely replicate our findings regarding microgliosis and microglial *Dkk2* upregulation in two widely used AD mouse models ($APP^{NL\text{-}G\text{-}F}$ and *APP/PS1* mice), again adding spatial information to a previously published meta-analysis of single-cell RNA-Seq datasets (Friedman et al., 2018). However, the lack of βAmyloid plaques and microglial phenotype in hippocampal CA1 *stratum pyramidale* proximal regions of the *APP/PS1* mouse evokes the notion that the microglial phenotype investigated here could be linked to plaque proximity.

Dkk2^{+} microglia exhibit increased propensity for clustering around βAmyloid plaques

To investigate whether *Dkk2* expression status was correlated with βAmyloid plaque proximity, we performed nearest neighbour analysis to quantify the spatial relationship between microglia and the nearest βAmyloid plaque dense core identified following βAmyloid IHC in *APP*$^{NL\text{-}G\text{-}F}$ and *APP/PS1* mice (schematic shown in Fig. 3*A*). Frequency distributions of recorded distances were summarised in histograms. In AD mouse models, we distinguished between *Dkk2*$^{+}$ and *Dkk2*$^{-}$ microglia, whereas no such distinction was made in wild-type mice as *Dkk2* expression levels were negligible at all time points (Fig. 1*A*,*B*,*F*,*J*, 2*A*,*B*,*E*,*I*). Furthermore, where no plaques were evident (e.g., in wild-type or pre-disease stage mice or in some hippocampal CA1 *stratum pyramidale* proximal regions) distances to plaque dense core "placeholders" randomly placed on confocal images were measured instead.

As would be expected, wild-type littermate controls of *APP*$^{NL\text{-}G\text{-}F}$ mice used in our study exhibited microglia at varying/random distances to the nearest randomly assigned dense core placeholder in the motor cortex and CA1 hippocampus at 7 and 24 months (Fig. 1*A,B*, 3*B-E*). This finding is in keeping with the homogeneous tiling behaviour usually exhibited by microglia in the healthy CNS (Nimmerjahn et al., 2005). In stark contrast, a large proportion of *Dkk2*$^{+}$ and *Dkk2*$^{-}$ microglia were found within 20 µm of the nearest plaque dense core in the cortex of 7 months old *APP*$^{NL\text{-}G\text{-}F}$ mice, while *Dkk2*$^{+}$ microglia were predominantly located within 40 µm of plaque dense cores in the CA1 hippocampus (Fig. 3*B,D*). By 24 months, the clustering of microglia around βAmyloid plaque dense cores, especially that of *Dkk2*$^{+}$ microglia, became even more pronounced both in the cortex and in the CA1 hippocampus (Fig. 3*C,D*). Skewness and kurtosis analyses of histogram distribution curves for each individual animal revealed that *APP*$^{NL\text{-}G\text{-}F}$ microglia were statistically significantly more tightly clustered around plaque dense cores with increasing age than microglia of age-matched control mice (Fig. 3-1A-H). Crucially however, in 24 months old *APP*$^{NL\text{-}G\text{-}F}$ mice, *Dkk2*$^{+}$ microglia were statistically significantly more tightly associated with plaques than *Dkk2*$^{-}$

570 microglia both in the cortex and in the CA1 hippocampus (Fig. 3-1C,D,G,H; One-Way
571 ANOVA [n]).

572 We observed similar plaque-microglia distance relationships in *APP/PS1* mice and
573 respective wild-type littermate controls. Microglia in the wild-type littermate control mouse
574 cortex and CA1 hippocampus were evenly distributed relative to the nearest randomly
575 placed plaque dense core placeholder (Fig. 3*F-K*). In the cortex of 3 months old (pre disease
576 stage and plaque free) *APP/PS1* mice, both *Dkk2*$^{+}$ and *Dkk2*$^{-}$ microglia exhibited similar
577 wild-type-like distance distributions (Fig. 3*F*), whereas microglia increasingly clustered within
578 20 µm of plaque dense cores at subsequent (disease stage) time points, with *Dkk2*$^{+}$
579 microglia exhibiting slightly more pronounced clustering versus *Dkk2*$^{-}$ microglia at 12 months
580 (Fig. 3*G,H*); we note that the latter difference was not statistically significant according to
581 skewness and kurtosis analysis, while clustering of *Dkk2*$^{+}$ microglia around plaques dense
582 cores in *APP/PS1* mice was statistically significantly increased versus that of microglia of
583 age-matched control mice from 8 months onwards (Fig. 3-1I-N; One-Way ANOVA [o]). As
584 discussed above, due to the small amounts of βAmyloid plaques in hippocampal CA1
585 *stratum pyramidale* proximal regions of the *APP/PS1* mouse, microglia distributions were
586 comparatively variable, especially at 3 months (Fig. 3*I*), even though substantial clustering of
587 *Dkk2*$^{+}$ microglia was registered in those instances were βAmyloid plaques were observed in
588 CA1 *stratum pyramidale* proximal regions at 8 and 12 months (Fig. 3*J,K*). Accordingly,
589 skewness and kurtosis analyses were inconclusive for CA1 microglia (Fig. 3-1O-T; One-Way
590 ANOVA [p]).

591 While it is widely known that microglia accumulate around CNS lesions such as βAmyloid
592 plaques, our data further suggest that clustering around plaques is frequently accompanied
593 by the expression of *Dkk2*, especially in the *APP*$^{NL\text{-}G\text{-}F}$ AD mouse model. Conversely, in the
594 healthy brain, microglia were evenly tiled and lacked *Dkk2* expression.

595

Microgliosis and microglial *Dkk2* upregulation in *SOD1^{G93A}* ALS mice

Having demonstrated microgliosis and clustering of *Dkk2*$^{+}$ microglia around βAmyloid plaques in two different widely used AD mouse models, we next investigated whether our findings could be recapitulated in another neurodegeneration mouse model, the *SOD1^{G93A}* amyotrophic lateral sclerosis (ALS) mouse (Gurney et al., 1994). According to the meta-analysis of single-cell RNA-Seq datasets by Friedman et al., 2018, microglial *Dkk2* upregulation should also be evident in this mouse model. It expresses the mutant human *SOD1^{G93A}* gene that causes motor neuron degeneration in the spinal cord and other parts of the CNS, which underlies ALS (Gurney et al., 1994). We performed mRNA FISH to detect microglial *Dkk2* mRNA *in situ* paired with immunohistochemical labelling using an antibody against Iba1 on transverse cryosections from the lumbar (L)5 region of the spinal cord and acquired images from the ventral horn, an area that displays robust motor neuron degeneration in this mouse model (Gurney et al., 1994),

In control mice expressing wild-type human *SOD1 (SOD1^{WT})*, but not in age-matched mice expressing *SOD1^{G93A},* no overt changes in microgliosis and *Dkk2* expression were observed at any of the assessed time points (Fig. 1*A-E*). At the early 50 days time point, *SOD1^{G93A}* mice still exhibited control levels of microgliosis (1.7 ± 0.1 versus 1.6 ± 0.2 DAPI^{+}/Iba1^{+} microglia per FOV (Fig. 4*A*,*B*), 244.7 ± 73.2 vs 266.5 ± 59.7 µm^2 Iba1 area (Fig. 4*A*,*C*)). However, the number of microglia was significantly elevated in *SOD1^{G93A}* compared with age-matched control *SOD1^{WT}* mice at 100 days (6.3 ± 0.9 vs. 1.8 ± 0.2) and at 120 days (13.6 ± 0.9 vs. 1.5 ± 0.4) (Fig. 4*A*,*B*; Two-Way ANOVA, $p < 0.0001$ (timepoints) and $p = 0.0001$ (genotypes) [q]). Accordingly, the area of Iba1 immunoreactivity was also significantly higher in *SOD1^{G93A}* versus *SOD1^{WT}* mice at 100 days (918.8 ± 31.7 vs. 328.1 ± 75.3 µm^2) and at 120 days (1646.0 ± 184.7 vs. 248.7 ± 42.1 µm^2) (Fig. 4*A*,*C*; Two-Way ANOVA, $p < 0.0001$ (timepoints) and $p = 0.0001$ (genotypes) [r]). *Dkk2* expression per microglial cell progressively increased in *SOD1^{G93A}* but not in *SOD1^{WT}* mice, although this increase only reached significance at 120 days: 0.8 ± 0.7 µm^2, 2.4 ± 0.8 µm^2, and 10.7 ± 4.6 µm^2 in

SOD1^{G93A} mice at 50/100/120 days; 0.7 ± 0.5 µm^2, 0.5 ± 0.3 µm^2, and 0.5 ± 0.6 µm^2 in *SOD1*^{WT} mice at 50/100/120 days (Fig. 4*A*,*D*; Two-Way ANOVA, p = 0.0154 (timepoints) and p = 0.0193 (genotypes) [s]). Thus, fast-paced microgliosis is evident between 50 and 100 days in *SOD1*^{G93A} mice, with a slightly reduced rate of acceleration between 100 days and 120 days (Fig. 4*E*). Conversely, microglial *Dkk2* upregulation appears to accelerate especially in the final pathological stages. This resulted in a relative contribution of *Dkk2*$^+$ microglia versus total microglia that was significantly increased in *SOD1*^{G93A} compared to *SOD1*^{WT} mice: 45.4 ± 5.1 %, 56.5 ± 19.2 %, and 75.0 ± 4.4 % in *SOD1*^{G93A} mice at 50/100/120 days; 39.9 ± 17.4 %, 27.5 ± 14.3 %, and 14.6 ± 3.6 % in *SOD1*^{WT} mice at 50/100/120 days (Fig. 4-1*A*; Two-Way ANOVA, p = 0.9125 (timepoints) and p = 0.0073 (genotypes) [t])

We next sought to investigate whether microgliosis and microglial *Dkk2* upregulation in the *SOD1*^{G93A} ALS mouse model were spatially correlated with local CNS lesions, analogous to that observed in the *APP*$^{NL-G-F}$ and *APP/PS1* AD mouse models. In absence of AD-typical βAmyloid plaques in ALS, we combined *Dkk2* mRNA FISH and microglial immunohistochemical labelling with the immunolabelling of GFAP to visualise astrocytes and immunolabelling of misfolded SOD1 to visualise aggregates of misfolded mutant SOD1^{G93A}. In 120 days old *SOD1*^{G93A} ALS mice, we failed to detect clustering of microglia, irrespective of their Dkk2 expression status, specifically around GFAP (Fig. 4*F*). However, we observed some degree of microglial clustering around misfolded SOD1 immunoreactivity (Fig. 4*G,H;* magenta regions of interest (ROIs)). However, many microglia did not exhibit local accumulation around misfolded SOD1 lesions (Fig. 4*G,H*: cyan ROIs). In absence of a clear clustering pattern, these observations were not quantified.

Taken together, the microgliosis and microglial *Dkk2* upregulation detected in the brains of AD mouse models could also be replicated in an unrelated neurodegeneration mouse model, namely in the spinal cord of the *SOD1*^{G93A} ALS mice. While some degree of clustering around misfolded SOD1 aggregates occurred, this was not as robust as the clustering around βAmyloid plaques in the *APP*$^{NL-G-F}$ and *APP/PS1* AD mouse models.

650 Nonetheless, our findings support the published notion that *Dkk2* upregulation may be part
651 of a general response in CNS microglia as they transition from surveillance to activation
652 (DAM/ARM microglia), at least in mouse models of neurodegeneration (Friedman et al.,
653 2018; Sala Frigerio et al., 2019; Meilandt et al., 2020). This supports the possibility that *Dkk2*
654 represents a DAM/ARM marker gene, at least in mice.

655

DKK2 recombinant protein disrupts WNT7a-induced synapse features in cultured neurons

We next sought to investigate what effect Dkk2 protein secreted by microglia might have on its surroundings under the assumption that increased microglial *Dkk2* expression at the mRNA level results in increased microglial Dkk2 protein secretion. We focused our study on synapses in mature primary neuron cultures due to the well-known anti-synaptic effect that the Dkk2 homologue Dkk1 has on them, which it brings about by decreasing canonical and increasing non-canonical Wnt signalling (Purro et al., 2012; Galli et al., 2014; Marzo et al., 2016; Elliott et al., 2018; Sellers et al., 2018). However, we note that, in principle, Dkk2 can have context-dependent agonistic and antagonistic effects (Mao and Niehrs, 2003).

To this end, we treated mature rat hippocampal neuron cultures sparsely expressing *hSyn:EGFP* at 21 days *in vitro* with recombinant proteins for 24 hrs (WNT7a, 200 ng/ml; DKK1, 100 ng/ml; DKK2, 100 ng/ml; DKK2 + WNT7a, 100 and 200 ng/ml; BSA control, 100 ng/ml). Chosen recombinant protein concentrations were in line with published works and/or TCF/LEF dose dependence assays performed in house (data not shown). This was followed by immunocytochemical labelling using antibodies against the pre- and post-synaptic markers vGlut and Homer. A typical sparsely labelled (*hsyn:EGFP*$^{+}$) neuron with highlighted primary dendrite (boxed ROI) that was used for analysis is depicted in Fig. 5*A*. WNT7a treatment significantly increased the number of dendritic spines as well as the number of post-synaptic homer puncta compared with BSA treatment (Fig. 5*B,C,G,H;* One-Way ANOVA, dendritic spines: $p = 0.0023$ [u]; homer puncta: $p = 0.0309$ [v]). Conversely, these metrics were unaffected by DKK1 and DKK2 treatment (Fig. 5*D,E,G,H;* One-Way ANOVA; all n.s.) and crucially also by combined DKK2 + WNT7a treatment (Fig. 5*F,G,H;* One-Way ANOVA; n.s.). The absolute number of synapses (defined as Homer/vGlut apposition events with up to 1 µm distance) was similarly increased by WNT7a but not by DKK1, DKK2 or a combination of DKK2 and WNT7a compared with BSA, although this did not reach statistical significance (Fig. 5*I*; One-Way ANOVA; n.s.).

683 Nonetheless, these combined data suggest that DKK2 treatment is antagonistic rather than
684 agonistic and completely abolishes the pro-synaptogenic effect of WNT7a treatment, at least
685 in our *in vitro* assay. Furthermore, it appears that the antagonistic effect of DKK2 as well as
686 that of the established Wnt signalling antagonist DKK1 rely upon an inherent Wnt signalling
687 tone that was low/absent in our cultures, as neither reduced synaptic metrics to levels below
688 those found with BSA treatment when applied independently.

689

690 **_DKK2_ is not upregulated in human microglia**

691 We have thus far demonstrated significant microgliosis and microglial *Dkk2* upregulation in
692 AD and ALS mouse models of neurodegeneration, as well as clustering of *Dkk2*$^{+}$ microglia
693 around βAmyloid plaques. In combination with previously published studies, which have
694 demonstrated microglial *Dkk2* upregulation by single-cell RNA-Seq (Friedman et al., 2018;
695 Sala Frigerio et al., 2019; Meilandt et al., 2020), this led us to postulate that *Dkk2* may
696 represent a *bona fide* DAM/ARM marker gene at least in neurodegeneration mouse models.
697 We next sought to investigate whether our findings were recapitulated in human subjects
698 diagnosed with AD.

699 To analyse microglial *DKK2* expression in humans, we obtained human *post-mortem* frontal
700 cortex brain tissue from healthy control individuals, as well as individuals diagnosed with AD
701 and pathological ageing, the latter being defined as non-demented individuals with AD-
702 typical histopathologic changes. Demographic data and post-mortem brain assessments are
703 summarised in Table 6-1. We performed mRNA FISH to detect *DKK2* mRNA in microglia
704 that were additionally labelled by mRNA FISH for the microglial markers *TREM2* and
705 *P2RY12* (see also Table 6-2 for added analysis parameters). This was paired with
706 immunohistochemical labelling using an antibody against βAmyloid to label βAmyloid
707 plaques. As expected, samples from control individuals were devoid of βAmyloid plaques
708 while those classified “pathological ageing” and “AD” exhibited progressively increasing
709 levels of plaque burden (Fig. 6*A-C*). However, we did not detect significant differences in the
710 number of DAPI^{+}/*TREM2*$^{+}$/*P2RY12*$^{+}$ microglia per field of view between control, pathological
711 ageing, and AD groups (Fig. 6*A-D*; control: 11.1 ± 10.7 microglia / FOV; pathological ageing:
712 6.2 ± 3.4; AD: 8.0 ± 6.8; one-way ANOVA, p = 0.4507 ^{w}). This absence of microglia number
713 changes is in line with findings from published literature (e.g.: Marlatt et al., 2014; Davies et
714 al., 2017; Paasila et al., 2019; Franco-Bocanegra et al., 2021). Similarly, *DKK2* expression
715 per DAPI^{+}/*TREM2*$^{+}$/*P2RY12*$^{+}$ microglial cell did not differ between control (0.5 ± 0.2 μm^{2}),
716 pathological ageing (0.7 ± 0.1 μm^{2}), and AD groups (0.7 ± 0.4 μm^{2}) (Fig. 6*A-C,E;* one-way

ANOVA, p = 0.7689 [x]). This was accompanied by unchanged relative contributions of *DKK2*$^+$ microglia across control (38.3 ± 9.7 %), pathological ageing (38.3 ± 3.8%), and AD groups (41.6 ± 12.5 %) (Fig. 6-1*A;* One-Way ANOVA, p = 0.8650 [y]). We further found that *DKK2* expression status had no effect on *TREM2* expression levels per DAPI$^+$/*TREM2*$^+$/*P2RY12*$^+$ microglial cell in control (*DKK2*$^+$: 0.8 ± 0.3 µm^2 ; *DKK2*$^-$: 0.6 ± 0.3 µm^2), pathological ageing (*DKK2*$^+$: 0.9 ± 0.9 µm^2; *DKK2*$^-$: 0.7 ± 0.2 µm^2), and AD individuals (*DKK2*$^+$: 0.5 ± 0.2 µm^2; *DKK2*$^-$: 0.4 ± 0.2 µm^2) (Fig. 6-1*B;* one-way ANOVA, p = 0.2349 [z]). Conversely, *P2RY12* expression levels per DAPI$^+$/*TREM2*$^+$/*P2RY12*$^+$ microglial cell were increased in cells co-expressing *DKK2* compared with cells that lacked *DKK2* expression, although that difference was not statistically significant: control (*DKK2*$^+$: 2.7 ± 1.0 µm^2; *DKK2*$^-$: 1.7 ± 0.5 µm^2), pathological ageing (*DKK2*$^+$: 2.7 ± 0.5 µm^2; *DKK2*$^-$: 2.0 ± 0.9 µm^2), and AD individuals (*DKK2*$^+$: 3.2 ± 1.6 µm^2; *DKK2*$^-$: 1.6 ± 0.8 µm^2) (Fig. 6-1*C;* One-Way ANOVA, p = 0.1056 [ab]).

We subsequently assessed the clustering behaviour of microglia around βAmyloid plaques. In healthy control individuals, the total microglia population displayed a varying/random spatial distribution around the nearest randomly placed dense core placeholder, which furthermore did not appear to be modified by *DKK2* expression status (Fig. 6*A,F*). In individuals classified as “pathological ageing”, we identified emerging populations of both *DKK2*$^+$ and *DKK2*$^-$ microglia that frequently accumulated around βAmyloid plaque dense cores up to a distance of 50 µm, although clustering in the proximal most regions was more robust for *DKK2*$^-$ cells (Fig. 6*B,G*). This clustering was further consolidated, especially among *DKK2*$^+$ microglia, whose predominant distribution now also included proximal most regions (Fig. 6*C,H*).

Taken together, our data on human frontal cortex post-mortem tissue indicate that neither the increase in microglial numbers nor microglial *DKK2* upregulation, both of which were evident in mouse models, occur in human brains under conditions classified as “pathological ageing” and “AD”. However, microglia did exhibit clustering behaviour around βAmyloid plaques even though this was not linked to *DKK2* expression.

744

745 **Discussion**

746 Past and present research have linked dysregulated Wnt signalling to AD (e.g. Palomer et
747 al., 2022; previously reviewed by Purro et al., 2014; Palomer et al., 2019; Aghaizu et al.,
748 2020; Inestrosa et al., 2021). However, recent research has also more intimately linked
749 microglia and neuroinflammation to AD, as initially exemplified by variants of genes
750 predominantly expressed in microglia like *TREM2* and *CD33* exhibiting disease modifying
751 properties (Bradshaw et al., 2013; Guerreiro et al., 2013). New evidence even suggests that
752 the microglial AD response is itself regulated by Wnt signalling, as the signalling pathway
753 downstream of TREM2, essential for regulating microglial survival and proliferation, cross-
754 talks with the Wnt pathway (Zheng et al., 2017; Meilandt et al., 2020).

755 Here we sought to explore the role of *DKK2/Dkk2*, which encodes a Wnt signalling
756 modulator, that was upregulated in a subpopulation of microglia (DAM/ARM) in various
757 single and bulk cell RNA-Seq studies on neurodegeneration mouse models (Friedman et al.,
758 2018; Sala Frigerio et al., 2019; Meilandt et al., 2020). Our histological data obtained largely
759 by mRNA FISH combined with immunocytochemistry replicated the findings cited above.
760 Crucially however, we added valuable spatial information on the location of *Dkk2*$^{+}$ microglia
761 with respect to neurodegenerative lesions such as βAmyloid plaques in AD mouse models,
762 where *Dkk2*$^{+}$ microglia exhibited a potential to cluster near βAmyloid plaques that was
763 greater or at least equal to that of *Dkk2*$^{-}$ microglia, at least in advanced- *APP*$^{NL\text{-}G\text{-}F}$ mice. The
764 exact role of Dkk2 protein expression is yet to be fully understood, but assuming its reported
765 role as a secreted, soluble protein (reviewed by Niehrs, 2006) we speculated that Dkk2's
766 mechanism of action could be autocrine or paracrine in nature. In support of the former,
767 oncological evidence suggests that peripheral immune natural killer and CD8^{+} T cells, which
768 are derived from the same myeloid lineage as CNS microglia, can detect soluble Dkk2.
769 However, in this context, Dkk2 was utilised as an immune evasion tool secreted by tumours
770 to suppress cytotoxic immune cell activation and tumour destruction via an atypical, Wnt

771 signalling independent pathway (Xiao et al., 2018). Nonetheless, it is a possibility that
772 microglial-derived Dkk2 can also act upon microglia in an autocrine fashion at least in mice,
773 although we can only speculate what the cellular response to such a stimulus would be.

774 Conversely, we provide evidence in support of a paracrine mechanism at least in cultured rat
775 primary neurons as we demonstrate that recombinant human DKK2 protein blocks the
776 synaptogenic effect of Wnt *in vitro*. However, we note that the administered DKK2 protein
777 concentration may not match physiological, microglia derived Dkk2/DKK2 protein levels *in*
778 *situ*. Knowing that DKK2 can generally engage in Wnt antagonising and agonising activities
779 depending respectively on the presence or absence of the co-receptor Kremen2 (Mao and
780 Niehrs, 2003), it appears that, at least in our *in vitro* system, DKK2 protein acts as an
781 antagonist. DKK2 may thus behave similarly to DKK1, a negative regulator of canonical
782 Wnt/β-catenin and non-canonical Wnt/PCP signalling with known synapse destabilising
783 properties (Purro et al., 2012; Galli et al., 2014; Killick et al., 2014; Marzo et al., 2016; Elliott
784 et al., 2018; Sellers et al., 2018; see also review by Aghaizu et al., 2020), likely also in the
785 human AD brain (Caricasole et al., 2004). Synapse density reductions in plaque proximal
786 regions (Koffie et al., 2009) would be consistent with the fact that oligomeric βAmyloid
787 induces *Dkk1* expression (Purro et al., 2012; Killick et al., 2014; Jackson et al., 2019). *Dkk2*$^{+}$
788 microglia accumulating around βAmyloid plaques may locally increase Dkk2 protein levels,
789 adding to the anti-synaptic milieu established by Dkk1 near plaques. Given that microglia
790 already engage in complement-mediated synaptic pruning by phagocytosis in AD mouse
791 models (Hong et al., 2016; Shi et al., 2017), the relative contributions of individual
792 synaptotoxic components around plaques will have to be addressed in future studies.

793 In assessing the chronological order between microgliosis/microglial plaque clustering and
794 microglial *Dkk2* upregulation, we observed significant microgliosis increases before *Dkk2*
795 upregulation in *APP/PS1*, *APP*$^{NL\text{-}G\text{-}F}$, and *SOD1*^{G93A} mice with respect to absolute
796 quantification metrics (see Fig 1,2,4). However, when comparing relative rate changes, the
797 rate of *Dkk2* signal increase at early disease stages in the *APP/PS1* AD mouse model

surpassed the rate of microgliosis increase (Fig. 2*F,J*). It should be noted that *Dkk2* induction was initiated from near-zero basal expression levels (Fig. 2*E*), whereas both basal microglia numbers and Iba1 immunoreactivity levels were decidedly greater than zero (Fig. 2*C,D,G,H*). The potential for more pronounced changes was thus markedly greater for *Dkk2* induction at least in *APP/PS1* mice. Conversely, in *SOD1*^{G93A} ALS mice, the rate of microgliosis increase surpassed that of *Dkk2* signal increase at early disease stages (Fig. 4*E*). Presumably, basal microglial cell densities lower than those observed in the mouse brain (Fig. 4*B,C* vs 2*C,D,G,H*), which is in keeping with published literature (Tan et al., 2020), likely contributed at least partially to this outcome.

What should be addressed in future studies is whether the ability to induce *Dkk2* expression is innate in all microglia or whether context, such as proximity to neurodegenerative lesions, is to be ascribed a more prominent role. CNS microglia are not a homogeneous population of cells, with gene expression signatures differing depending on factors such as brain region, sex, age, and context including disease (reviewed by Masuda et al., 2020). In 3 month old *APP*$^{NL-G-F}$ mice, *Dkk2*$^{+}$ ARM cells represented 6 % of to the total microglial pool (Sala Frigerio et al., 2019); this number increased to 33 and 52 % at 6 months and 12 months respectively. It will be interesting to discern whether ARM-competence is restricted to the initial population of ARM cells, which then serve as a proliferating seed population, or whether cells from the total microglia pool are continuously recruited into the *Dkk2*$^{+}$ ARM population as disease progresses. The potential to produce *Dkk2*$^{+}$ ARM may further by influenced by other factors, which should be addressed in future studies, as different neurodegeneration disease models and CNS regions analysed in our study exhibited varying contributions of *Dkk2*$^{+}$ microglia relative to the total microglial pool.

Finally, our study has revealed discrepancies between human AD and transgenic AD mouse models. *DKK2* mRNA expression levels were not elevated in post-mortem frontal cortex samples from individuals diagnosed with AD vs healthy individuals. While other human brain and CNS regions like the motor cortex, hippocampus, and spinal cord might exhibit *DKK2*

upregulation (although unlikely given the absence of *DKK2* upregulation in recently published human RNA-seq databases; see below), the above finding is in stark contrast to our findings in neurodegeneration mouse models. In contrast to the situation in human patients, proximity to βAmyloid plaques appeared to be a strong predictor of microglial *Dkk2* expression in mice, both in the hippocampus and motor cortex. We note that those microglia that exhibited *DKK2* expression at the mRNA level in human tissue also displayed higher levels of the microglial marker *P2RY12*, but not *TREM2*. While the relevance of this finding is yet to be determined, published research has shown microglial expression of *P2RY12*, typically considered a homeostatic microglial marker gene, in proximity to diffuse plaques in post-mortem tissue from AD individuals (Walker et al., 2020). A caveat worth mentioning in relation to the lack of *DKK2* upregulation is the fact that human microglia at AD end stage (Braak & Braak stage 5-6) were chronically exposed to disease for much longer periods than their mouse counterparts and chronic adaptations in microglia gene expression signatures as well as microglial numbers may have masked potential earlier changes (we note that our pathological ageing samples at Braak & Braak stage 3-4 also lacked *DKK2* upregulation). Nevertheless, it is now known that gene expression signatures between mouse and human DAM/ARM populations, although overlapping to some extent, exhibit distinct differences (reviewed by Wang, 2021). In fact, numerous single-cell RNA-seq analyses have identified gene expression signatures that differed between mouse and human DAM/ARM populations (Grubman et al., 2019; Mathys et al., 2019; Nguyen et al., 2020; Olah et al., 2020; Smith et al., 2022). For technical reasons and in contrast to mouse studies, human single-cell RNA-seq studies are frequently, although not exclusively (Olah et al., 2020), restricted to nuclear transcripts, which may have contributed to the apparent transcriptomic differences between mouse and human microglia (note that extra-nuclear mRNA is abundant due to nuclear export before translation). However, even in a recent single nucleus RNA-seq comparative study involving human AD post-mortem tissue and the *5xFAD* AD mouse model, differences between human and mouse microglial gene expression signatures persisted (Zhou et al., 2020). The inability to detect extra-nuclear mRNA in human brain samples can be

853 circumvented with the use of optimised tissue harvesting protocols (Olah et al., 2020), or *in*
854 *situ* detection methods such as low throughput mRNA FISH (present study; Jolly et al.,
855 2019) or higher throughput digital spatial profiling (Prokop et al., 2019). Nonetheless, our
856 mRNA FISH based study strengthens the notion that human and mouse microglia, despite
857 exhibiting some overlaps, are different even beyond just the expression status of
858 *DKK2/Dkk2*, at least in the brain. Future studies should also examine any such interspecies
859 differences in the spinal cord.

860 Our study therefore highlights the increasingly recognised difficulties and limitations of using
861 mouse models to recapitulate facets of human biology and disease (Elder et al., 2010;
862 Jucker, 2010; Cavanaugh et al., 2014; Justice and Dhillon, 2016; Perlman, 2016; Dawson et
863 al., 2018). Regardless of whether this may be ascribed in our study to differing biological
864 responses in humans vs mice or masking chronic adaptations in much longer human
865 disease, these limitations likely play a key role in the absence of truly disease altering
866 therapies to date despite decades of AD research and >100 clinical trials. Future AD
867 research should thus substantially increase scrutiny in cases where animal models are to be
868 used to ensure faithful modelling of human biology. Human based AD models including
869 human induced pluripotent stem cell-derived cell cultures and brain organoids are potent
870 additions to our tool-kit despite still lacking the capacity to fully recapitulate human *in vivo*
871 biology in an *in vitro* setting, and indeed in an *in vivo* setting (Mancuso et al., 2019).

872

873 **References**

874 Aghaizu ND, Jin H, Whiting PJ (2020) Dysregulated Wnt Signalling in the Alzheimer's Brain.
875 Brain Sci 2020 10:902.

876 Bafico A, Liu G, Yaniv A, Gazit A, Aaronson SA (2001) Novel mechanism of Wnt signalling
877 inhibition mediated by Dickkopf-1 interaction with LRP6/Arrow. Nat Cell Biol 3:683–686.

878 Bradshaw EM, Chibnik LB, Keenan BT, Ottoboni L, Raj T, Tang A, Rosenkrantz LL,
879 Imboywa S, Lee M, Von Korff A, Morris MC, Evans DA, Johnson K, Sperling RA,
880 Schneider JA, Bennett DA, De Jager PL (2013) CD33 Alzheimer's disease locus:
881 Altered monocyte function and amyloid biology. Nat Neurosci 16:848–850.

882 Caricasole A, Copani A, Caraci F, Aronica E, Rozemuller AJ, Caruso A, Storto M, Gaviraghi
883 G, Terstappen GC, Nicoletti F (2004) Induction of Dickkopf-1, a Negative Modulator of
884 the Wnt Pathway, Is Associated with Neuronal Degeneration in Alzheimer's Brain. J
885 Neurosci 24:6021–6027.

886 Cavanaugh SE, Pippin JJ, Barnard ND (2014) Animal models of Alzheimer disease:
887 historical pitfalls and a path forward. ALTEX - Altern to Anim Exp 31:279–302.

888 Davies DS, Ma J, Jegathees T, Goldsbury C (2017) Microglia show altered morphology and
889 reduced arborization in human brain during aging and Alzheimer's disease. Brain
890 Pathol 27:795–808.

891 Dawson TM, Golde TE, Lagier-Tourenne C (2018) Animal models of neurodegenerative
892 diseases. Nat Neurosci 2018 2110 21:1370–1379.

893 Devotta A, Hong C-S, Saint-Jeannet J-P (2018) Dkk2 promotes neural crest specification by
894 activating Wnt/β-catenin signaling in a GSK3β independent manner. Elife 7.

895 Elder GA, Gama Sosa MA, De Gasperi R (2010) Transgenic mouse models of Alzheimer's
896 disease. Mt Sinai J Med 77:69–81.

897 Elliott C, Rojo AI, Ribe E, Broadstock M, Xia W, Morin P, Semenov M, Baillie G, Cuadrado
898 A, Al-Shawi R, Ballard CG, Simons P, Killick R (2018) A role for APP in Wnt signalling
899 links synapse loss with β-amyloid production. Transl Psychiatry 8:179.

900 Franco-Bocanegra DK, Gourari Y, McAuley C, Chatelet DS, Johnston DA, Nicoll JAR, Boche
901 D (2021) Microglial morphology in Alzheimer's disease and after Aβ immunotherapy.
902 Sci Reports 2021 111 11:1–12.

903 Friedman BA, Srinivasan K, Ayalon G, Meilandt WJ, Lin H, Huntley MA, Cao Y, Lee S-H,
904 Haddick PCG, Ngu H, Modrusan Z, Larson JL, Kaminker JS, van der Brug MP, Hansen
905 D V. (2018) Diverse Brain Myeloid Expression Profiles Reveal Distinct Microglial
906 Activation States and Aspects of Alzheimer's Disease Not Evident in Mouse Models.
907 Cell Rep 22:832–847.

908 Galli S, Lopes DM, Ammari R, Kopra J, Millar SE, Gibb A, Salinas PC (2014) Deficient Wnt
909 signalling triggers striatal synaptic degeneration and impaired motor behaviour in adult
910 mice. Nat Commun 5:1–13.

911 Gratuze M, Leyns CEG, Holtzman DM (2018) New insights into the role of TREM2 in
912 Alzheimer's disease. Mol Neurodegener 2018 131 13:1–16.

913 Grubman A, Chew G, Ouyang JF, Sun G, Choo XY, McLean C, Simmons RK, Buckberry S,
914 Vargas-Landin DB, Poppe D, Pflueger J, Lister R, Rackham OJL, Petretto E, Polo JM
915 (2019) A single-cell atlas of entorhinal cortex from individuals with Alzheimer's disease
916 reveals cell-type-specific gene expression regulation. Nat Neurosci 22:2087–2097.

917 Guerreiro R et al. (2013) *TREM2* Variants in Alzheimer's Disease. N Engl J Med 368:117–
918 127.

919 Gurney ME, Pu H, Chiu AY, Dal Canto MC, Polchow CY, Alexander DD, Caliendo J, Hentati
920 A, Kwon YW, Deng H-X, Chen W, Zhai P, Sufit RL, Siddique T (1994) Motor Neuron
921 Degeneration in Mice that Express a Human Cu,Zn Superoxide Dismutase Mutation.

Science 264:1772–1775.

Hirata H, Hinoda Y, Nakajima K, Kawamoto K, Kikuno N, Kawakami K, Yamamura S, Ueno K, Majid S, Saini S, Ishii N, Dahiya R (2009) Wnt Antagonist Gene DKK2 Is Epigenetically Silenced and Inhibits Renal Cancer Progression through Apoptotic and Cell Cycle Pathways. Clin Cancer Res 15:5678–5687.

Hong S, Beja-Glasser VF, Nfonoyim BM, Frouin A, Li S, Ramakrishnan S, Merry KM, Shi Q, Rosenthal A, Barres BA, Lemere CA, Selkoe DJ, Stevens B (2016) Complement and microglia mediate early synapse loss in Alzheimer mouse models. Science 352:712–716.

Inestrosa NC, Tapia-Rojas C, Cerpa W, Cisternas P, Zolezzi JM (2021) WNT Signaling Is a Key Player in Alzheimer's Disease. Handb Exp Pharmacol 269:357–382.

Jackson RJ, Rose J, Tulloch J, Henstridge C, Smith C, Spires-Jones TL (2019) Clusterin accumulates in synapses in Alzheimer's disease and is increased in apolipoprotein E4 carriers. Brain Commun 1:1–12.

Jankowsky JL, Fadale DJ, Anderson J, Xu GM, Gonzales V, Jenkins NA, Copeland NG, Lee MK, Younkin LH, Wagner SL, Younkin SG, Borchelt DR (2004) Mutant presenilins specifically elevate the levels of the 42 residue β-amyloid peptide in vivo: evidence for augmentation of a 42-specific γ secretase. Hum Mol Genet 13:159–170.

Jolly S, Lang V, Koelzer VH, Sala Frigerio C, Magno L, Salinas PC, Whiting P, Palomer E (2019) Single-Cell Quantification of mRNA Expression in The Human Brain. Sci Rep 9:12353.

Jucker M (2010) The benefits and limitations of animal models for translational research in neurodegenerative diseases. Nat Med 2010 1611 16:1210–1214.

Justice MJ, Dhillon P (2016) Using the mouse to model human disease: increasing validity and reproducibility. Dis Model Mech 9:103.

947 Keaveney MK, Tseng H an, Ta TL, Gritton HJ, Man HY, Han X (2018) A MicroRNA-Based
948 Gene-Targeting Tool for Virally Labeling Interneurons in the Rodent Cortex. Cell Rep
949 24:294–303.

950 Keren-Shaul H, Spinrad A, Weiner A, Matcovitch-Natan O, Dvir-Szternfeld R, Ulland TK,
951 David E, Baruch K, Lara-Astaiso D, Toth B, Itzkovitz S, Colonna M, Schwartz M, Amit I
952 (2017) A Unique Microglia Type Associated with Restricting Development of
953 Alzheimer's Disease. Cell 169:1276-1290.e17.

954 Killick R et al. (2014) Clusterin regulates β-amyloid toxicity via Dickkopf-1-driven induction of
955 the wnt-PCP-JNK pathway. Mol Psychiatry 19:88–98.

956 Koffie RM, Meyer-Luehmann M, Hashimoto T, Adams KW, Mielke ML, Garcia-Alloza M,
957 Micheva KD, Smith SJ, Kim ML, Lee VM, Hyman BT, Spires-Jones TL (2009)
958 Oligomeric amyloid β associates with postsynaptic densities and correlates with
959 excitatory synapse loss near senile plaques. Proc Natl Acad Sci U S A 106:4012–4017.

960 Kuphal S, Lodermeyer S, Bataille F, Schuierer M, Hoang BH, Bosserhoff AK (2006)
961 Expression of Dickkopf genes is strongly reduced in malignant melanoma. Oncogene
962 25:5027–5036.

963 Maehata T, Taniguchi H, Yamamoto H, Nosho K, Adachi Y, Miyamoto N, Miyamoto C,
964 Akutsu N, Yamaoka S, Itoh F (2008) Transcriptional silencing of Dickkopf gene family
965 by CpG island hypermethylation in human gastrointestinal cancer. World J
966 Gastroenterol 14:2702–2714.

967 Mancuso R, Van Den Daele J, Fattorelli N, Wolfs L, Balusu S, Burton O, Liston A, Sierksma
968 A, Fourne Y, Poovathingal S, Arranz-Mendiguren A, Sala Frigerio C, Claes C, Serneels
969 L, Theys T, Perry VH, Verfaillie C, Fiers M, De Strooper B (2019) Stem-cell-derived
970 human microglia transplanted in mouse brain to study human disease. Nat Neurosci
971 22:2111–2116.

Mao B, Niehrs C (2003) Kremen2 modulates Dickkopf2 activity during Wnt/lRP6 signaling. Gene 302:179–183.

Mao B, Wu W, Li Y, Hoppe D, Stannek P, Glinka A, Niehrs C (2001) LDL-receptor-related protein 6 is a receptor for Dickkopf proteins. Nature 411:321–325.

Marlatt MW, Bauer J, Aronica E, Van Haastert ES, Hoozemans JJM, Joels M, Lucassen PJ (2014) Proliferation in the Alzheimer Hippocampus Is due to Microglia, Not Astroglia, and Occurs at Sites of Amyloid Deposition. Neural Plast 2014:693851.

Marzo A, Galli S, Lopes D, McLeod F, Podpolny M, Segovia-Roldan M, Ciani L, Purro SA, Cacucci F, Gibb A, Salinas PC (2016) Reversal of Synapse Degeneration by Restoring Wnt Signaling in the Adult Hippocampus. Curr Biol 26:2551–2561.

Masuda T, Sankowski R, Staszewski O, Prinz M (2020) Microglia Heterogeneity in the Single-Cell Era. Cell Rep 30:1271–1281.

Mathys H, Davila-Velderrain J, Peng Z, Gao F, Mohammadi S, Young JZ, Menon M, He L, Abdurrob F, Jiang X, Martorell AJ, Ransohoff RM, Hafler BP, Bennett DA, Kellis M, Tsai LH (2019) Single-cell transcriptomic analysis of Alzheimer's disease. Nature 570:332–337.

Meilandt WJ et al. (2020) Trem2 Deletion Reduces Late-Stage Amyloid Plaque Accumulation, Elevates the Aβ42:Aβ40 Ratio, and Exacerbates Axonal Dystrophy and Dendritic Spine Loss in the PS2APP Alzheimer's Mouse Model. J Neurosci 40:1956–1974.

Mu J, Hui T, Shao B, Li L, Du Z, Lu L, Ye L, Li S, Li Q, Xiao Q, Qiu Z, Zhang Y, Fan J, Ren G, Tao Q, Xiang T (2017) Dickkopf-related protein 2 induces G0/G1 arrest and apoptosis through suppressing Wnt/β-catenin signaling and is frequently methylated in breast cancer. Oncotarget 8:39459.

Nguyen AT, Wang K, Hu G, Wang X, Miao Z, Azevedo JA, Suh ER, Van Deerlin VM, Choi

997 D, Roeder K, Li M, Lee EB (2020) APOE and TREM2 regulate amyloid-responsive
998 microglia in Alzheimer's disease. Acta Neuropathol 140:477–493.

999 Niehrs C (2006) Function and biological roles of the Dickkopf family of Wnt modulators.
1000 Oncogene 25:7469–7481.

1001 Nimmerjahn A, Kirchhoff F, Helmchen F (2005) Neuroscience: Resting microglial cells are
1002 highly dynamic surveillants of brain parenchyma in vivo. Science 308:1314–1318.

1003 Olah M et al. (2020) Single cell RNA sequencing of human microglia uncovers a subset
1004 associated with Alzheimer's disease. Nat Commun 2020 111 11:1–18.

1005 Paasila PJ, Davies DS, Kril JJ, Goldsbury C, Sutherland GT (2019) The relationship
1006 between the morphological subtypes of microglia and Alzheimer's disease
1007 neuropathology. Brain Pathol 29:726–740.

1008 Palomer E, Buechler J, Salinas PC (2019) Wnt Signaling Deregulation in the Aging and
1009 Alzheimer's Brain. Front Cell Neurosci 13:227.

1010 Palomer E, Martín-Flores N, Jolly S, Pascual-Vargas P, Benvegnù S, Podpolny M, Teo S,
1011 Vaher K, Saito T, Saido TC, Whiting P, Salinas PC (2022) Epigenetic repression of Wnt
1012 receptors in AD: a role for Sirtuin2-induced H4K16ac deacetylation of Frizzled1 and
1013 Frizzled7 promoters. Mol Psychiatry:1–10.

1014 Paolicelli RC et al. (2022) Microglia states and nomenclature: A field at its crossroads.
1015 Neuron 110:3458–3483.

1016 Perlman RL (2016) Mouse models of human disease: An evolutionary perspective. Evol Med
1017 Public Heal 2016:176.

1018 Prokop S, Miller KR, Labra SR, Pitkin RM, Hoxha K, Narasimhan S, Changolkar L,
1019 Rosenbloom A, Lee VMY, Trojanowski JQ (2019) Impact of TREM2 risk variants on
1020 brain region-specific immune activation and plaque microenvironment in Alzheimer's
1021 disease patient brain samples. Acta Neuropathol 138:613–630.

1022 Purro SA, Dickins EM, Salinas PC (2012) The secreted Wnt antagonist Dickkopf-1 is
1023 required for amyloid β-mediated synaptic loss. J Neurosci 32:3492–3498.

1024 Purro SA, Galli S, Salinas PC (2014) Dysfunction of Wnt signaling and synaptic disassembly
1025 in neurodegenerative diseases. J Mol Cell Biol 6:75–80.

1026 Rosi MC, Luccarini I, Grossi C, Fiorentini A, Spillantini MG, Prisco A, Scali C, Gianfriddo M,
1027 Caricasole A, Terstappen GC, Casamenti F (2010) Increased Dickkopf-1 expression in
1028 transgenic mouse models of neurodegenerative disease. J Neurochem 112:1539–
1029 1551.

1030 Rosner B (2015) Fundamentals of Biostatistics, 8th ed. Boston: Brooks Cole.

1031 Saito T, Matsuba Y, Mihira N, Takano J, Nilsson P, Itohara S, Iwata N, Saido TC (2014)
1032 Single App knock-in mouse models of Alzheimer's disease. Nat Neurosci 17:661–663.

1033 Sala Frigerio C, Wolfs L, Fattorelli N, Thrupp N, Voytyuk I, Schmidt I, Mancuso R, Chen W-
1034 T, Woodbury ME, Srivastava G, Möller T, Hudry E, Das S, Saido T, Karran E, Hyman B,
1035 Perry VH, Fiers M, De Strooper B (2019) The Major Risk Factors for Alzheimer's
1036 Disease: Age, Sex, and Genes Modulate the Microglia Response to Aβ Plaques. Cell
1037 Rep 27:1293-1306.e6.

1038 Sato H, Suzuki H, Toyota M, Nojima M, Maruyama R, Sasaki S, Takagi H, Sogabe Y, Sasaki
1039 Y, Idogawa M, Sonoda T, Mori M, Imai K, Tokino T, Shinomura Y (2007) Frequent
1040 epigenetic inactivation of DICKKOPF family genes in human gastrointestinal tumors.
1041 Carcinogenesis 28:2459–2466.

1042 Schindelin J, Arganda-carreras I, Frise E, Kaynig V, Longair M, Pietzsch T, Preibisch S,
1043 Rueden C, Saalfeld S, Schmid B, Tinevez J, White DJ, Hartenstein V, Eliceiri K,
1044 Tomancak P, Cardona A (2012) Fiji : an open-source platform for biological-image
1045 analysis. Nat Methods 9:676–682.

1046 Sellers KJ et al. (2018) Amyloid β synaptotoxicity is Wnt-PCP dependent and blocked by

1047 fasudil. Alzheimer's Dement 14:306–317.

1048 Shi Q, Chowdhury S, Ma R, Le KX, Hong S, Caldarone BJ, Stevens B, Lemere CA (2017)
1049 Complement C3 deficiency protects against neurodegeneration in aged plaque-rich
1050 APP/PS1 mice. Sci Transl Med 9:eaaf6295.

1051 Smith AM, Davey K, Tsartsalis S, Khozoie C, Fancy N, Tang SS, Liaptsi E, Weinert M,
1052 McGarry A, Muirhead RCJ, Gentleman S, Owen DR, Matthews PM (2022) Diverse
1053 human astrocyte and microglial transcriptional responses to Alzheimer's pathology.
1054 Acta Neuropathol 143:75–91.

1055 Tan YL, Yuan Y, Tian L (2020) Microglial regional heterogeneity and its role in the brain. Mol
1056 Psychiatry 25:351–367.

1057 Walker DG, Tang TM, Mendsaikhan A, Tooyama I, Serrano GE, Sue LI, Beach TG, Lue LF
1058 (2020) Patterns of Expression of Purinergic Receptor P2RY12, a Putative Marker for
1059 Non-Activated Microglia, in Aged and Alzheimer's Disease Brains. Int J Mol Sci 2020,
1060 Vol 21, Page 678 21:678.

1061 Wang H (2021) Microglia Heterogeneity in Alzheimer's Disease: Insights From Single-Cell
1062 Technologies. Front Synaptic Neurosci 13:68.

1063 Wang J, Tanila H, Puoliväli J, Kadish I, Van Groen T (2003) Gender differences in the
1064 amount and deposition of amyloidβ in APPswe and PS1 double transgenic mice.
1065 Neurobiol Dis 14:318–327.

1066 Xiao Q, Wu J, Wang WJ, Chen S, Zheng Y, Yu X, Meeth K, Sahraei M, Bothwell ALM, Chen
1067 L, Bosenberg M, Chen J, Sexl V, Sun L, Li L, Tang W, Wu D (2018) DKK2 imparts
1068 tumor immunity evasion through β-catenin-independent suppression of cytotoxic
1069 immune-cell activation. Nat Med 24:262–270.

1070 Zhang Y, Chen K, Sloan SA, Bennett ML, Scholze AR, O'Keeffe S, Phatnani HP, Guarnieri
1071 P, Caneda C, Ruderisch N, Deng S, Liddelow SA, Zhang C, Daneman R, Maniatis T,

1072 Barres BA, Wu JQ (2014) An RNA-sequencing transcriptome and splicing database of
1073 glia, neurons, and vascular cells of the cerebral cortex. J Neurosci 34:11929–11947.

1074 Zhang Y, Sloan SA, Clarke LE, Caneda C, Plaza CA, Blumenthal PD, Vogel H, Steinberg
1075 GK, Edwards MSB, Li G, Duncan JA, Cheshier SH, Shuer LM, Chang EF, Grant GA,
1076 Gephart MGH, Barres BA (2016) Purification and Characterization of Progenitor and
1077 Mature Human Astrocytes Reveals Transcriptional and Functional Differences with
1078 Mouse. Neuron 89:37–53.

1079 Zheng H, Jia L, Liu CC, Rong Z, Zhong L, Yang L, Chen XF, Fryer JD, Wang X, Zhang YW,
1080 Xu H, Bu G (2017) TREM2 promotes microglial survival by activating wnt/β-catenin
1081 pathway. J Neurosci 37:1772–1784.

1082 Zhou Y et al. (2020) Human and mouse single-nucleus transcriptomics reveal TREM2-
1083 dependent and TREM2-independent cellular responses in Alzheimer's disease. Nat
1084 Med 26:131–142.

1085 Zhu J, Zhang S, Gu L, Di W (2012) Epigenetic silencing of DKK2 and Wnt signal pathway
1086 components in human ovarian carcinoma. Carcinogenesis 33:2334–2343.

1087

1088

Figure legends

Figure 1. Microgliosis and microglial *Dkk2* upregulation in *APP*$^{NL\text{-}G\text{-}F}$ mice. *Dkk2* mRNA FISH as well as microglial Iba1 and βAmyloid IHC labelling in the motor cortex **(A)** and CA1 hippocampus **(B)** of *APP*$^{NL\text{-}G\text{-}F}$ mice**.** Boxed regions of interest (ROIs) were magnified for increased detail. **(C)** FIJI/ImageJ analysis workflow to quantifying punctated *Dkk2* mRNA FISH signal in Iba1-labelled (microglial) cells. Iba1 staining based analysis mask was generated, within which Dkk2 signal was quantified. **(D-G)** Microgliosis and *Dkk2* expression quantification in the *APP*$^{NL\text{-}G\text{-}F}$ motor cortex. **(D)** Quantification of microglia numbers per maximum projected field of view (FOV; 1.8 x 10^{-2} mm^2). **(E)** Iba1 IHC surface area per maximum projected FOV. **(F)** Normalised *Dkk2* mRNA FISH signal area per $DAPI^+/Iba^+$ microglial cell. **(G)** Comparative % changes of *Dkk2* expression and microglia numbers during time course. **(H-K)** Microgliosis and Dkk2 expression quantification in the *APP*$^{NL\text{-}G\text{-}F}$ CA1 hippocampus. **(H)** Quantification of microglia numbers per maximum projected FOV. **(I)** Iba1 IHC surface area per maximum projected FOV. **(J)** Normalised *Dkk2* mRNA FISH signal area per $DAPI^+/Iba^+$ microglial cell. **(K)** Comparative % changes of *Dkk2* expression and microglia numbers during time course. Individual data points represent the average of 4 FOVs analysed for each animal **(D-F, H-J)** or total averages from all animals per group **(G, K)**. N = 4 animals per condition and time point, n = 4 different fields of view / animal and brain region. Scale bars, (A-C) 25 µm; magnified ROIs: 5 µm. Two-way ANOVA with Multiple comparisons test. *p < 0.05; **p < 0.01; ***p < 0.001; ****p < 0.0001 ($^{a\text{-}f}$). See also Figure 1-1.

Figure 2. Microgliosis and microglial *Dkk2* upregulation in *APP/PS1* mice. *Dkk2* mRNA FISH as well as microglial Iba1 and βAmyloid IHC labelling in the motor cortex **(A)** and CA1 hippocampus **(B)** of *APP/PS1* mice**.** Boxed regions of interest (ROIs) were magnified for increased detail. **(C-F)** Microgliosis and *Dkk2* expression quantification in the *APP/PS1* motor cortex. **(C)** Quantification of microglia numbers per maximum projected FOV (FOV = 1.8 x 10^2 mm^2). **(D)** Iba1 IHC surface area per maximum projected FOV. **(E)** Normalised *Dkk2* mRNA FISH signal area per $DAPI^+/Iba^+$ microglial cell. **(F)** Comparative % changes of *Dkk2* expression and microglia numbers during time course. **(G-J)** Microgliosis and Dkk2 expression quantification in the *APP/PS1* CA1 hippocampus. **(G)** Quantification of microglia numbers per maximum projected FOV. **(H)** Iba1 IHC surface area per maximum projected FOV. **(I)** Normalised *Dkk2* mRNA FISH signal area per $DAPI^+/Iba^+$ microglial cell. **(K)** Comparative % changes of *Dkk2* expression and microglia numbers during time course. Individual data points represent the average of 4 FOVs analysed for each animal **(C-E, G-I)** or total averages from all animals per group **(F, J)**. N = 6 animals (3x females, 3x males) per time point and condition, n = 4 different fields of view / animal and brain region. Scale bars, (A-C) 25 µm; magnified ROIs: 5 µm. Two-way ANOVA with Multiple comparisons test. *p < 0.05; **p < 0.01; ***p < 0.001; ****p < 0.0001 ($^{i-k}$). See also Figure 2-1.

Figure 3. *Dkk2*$^{+}$ microglia cluster around βAmyloid plaques in *APP*$^{NL\text{-}G\text{-}F}$ and *APP/PS1* mice. (A) Schematic showing methodology of measuring distances between microglia and nearest βAmyloid plaque dense core. **(B-E)** Distribution of microglia (*Dkk2*$^{+}$, *Dkk2*$^{-}$ or total microglia (MG) populations) distances to nearest βAmyloid plaque dense core in *APP*$^{NL\text{-}G\text{-}F}$ or littermate control mice. Relative frequency distribution in the *APP*$^{NL\text{-}G\text{-}F}$ or control motor cortex at 7 months **(B)** and 24 months **(C)**. Relative frequency distribution in the *APP*$^{NL\text{-}G\text{-}F}$ or control CA1 hippocampus at 7 months **(B)** and 24 months **(C)**. **(F-K)** Distribution of microglia (*Dkk2*$^{+}$, *Dkk2*$^{-}$ or total microglia (MG) populations) distances to nearest βAmyloid plaque dense core in *APP/PS1* or littermate control mice. Relative frequency distribution in the *APP/PS1* or control motor cortex at 3 months **(F)**, 8 months **(G)**, and 12 months **(H)**. Relative frequency distribution in the *APP/PS1* or control CA1 hippocampus at 3 months **(I)**, 8 months **(J)**, and 12 months **(K)**. *APP*$^{NL\text{-}G\text{-}F}$/control: N = 4 animals per condition and time point, n = 4 different fields of view / animal and brain region; *APP/PS1*/control: N = 6 animals (3x females, 3x males) per time point and condition, n = 4 different fields of view / animal and brain region. See also Figure 3-1.

Figure 4. Microgliosis and microglial *Dkk2* upregulation in *SOD1^{G93A}* ALS mice. (A) *Dkk2* mRNA FISH and microglial Iba1 IHC labelling in the L5 spinal cord ventral horn of mice transgenically expressing human *SOD1^{WT}* (control) or mutant *SOD1^{G93A}* at 50, 100, and 120 days. Boxed regions of interest (ROIs) were magnified for increased detail. **(B)** Quantification of microglia numbers per maximum projected FOV (FOV = 1.8 x 10^{-2} mm^2). **(C)** Iba1 IHC surface area per maximum projected FOV. **(D)** Normalised *Dkk2* mRNA FISH signal area per $DAPI^+/Iba^+$ microglial cell. **(E)** Comparative % changes of *Dkk2* expression and microglia numbers during time course. **(F)** *Dkk2* mRNA FISH together with microglial Iba1 and astroglial GFAP IHC labelling in the L5 spinal cord ventral horn of 120 days old *SOD1^{G93A}* mice. **(G,H)** *Dkk2* mRNA FISH together with microglial Iba1 and misfolded SOD1 IHC labelling in the L5 spinal cord ventral horn of 120 days old *SOD1^{G93A}* mice. Magenta and cyan ROIs respectively depict proximity and absence of clear association between $DAPI^+/Iba1^+$ microglia and misfolded SOD1 foci. Individual data points represent the average of 4 FOVs analysed for each animal **(C-D)** or total averages from all animals per group **(E)**. N = 3 animals per time point and condition, n = 4 fields of view per animal. Scale bars, (A,F-H) 25 µm; magnified ROIs: 5 µm. Two-way ANOVA with Multiple comparisons test. *p < 0.05; **p < 0.01; ***p < 0.001; ****p < 0.0001 ($^{q-s}$). See also Figure 4-1.

Figure 5. Recombinant DKK2 protein neutralises the synaptogenic effect of WNT7a in mature hippocampal primary neurons. (A) Typical rat hippocampal neuron at DIV22 expressing *hSyn:EGFP* immunolabelled with Homer and vGlut. Boxed ROI indicates a primary dendritic branch, on which analysis in this section was focused. **(B-F)** Representative primary dendrites of DIV22 hippocampal neurons treated for 24 hrs with 100 ng/ml BSA control **(B)**,

200 ng/ml WNT7a **(C)**, 100 ng/ml DKK1 **(D)**, 100 ng/ml DKK2 **(E)**, and 100 ng/ml / 200 ng/ml DKK2 + WNT7a **(F)**. Immunolabelling for the pre- and post-synaptic markers vGlut and homer was performed, and merged views are shown in top panels. Remaining panels show homer (middle panel) and vGlut (lower panel) with outlined primary dendrite boundaries based on *hSyn:EGFP* labelling. **(G)** Normalised number of dendritic spines per 100 µm primary dendrite. **(H)** Normalised number of homer puncta per 100 µm primary dendrite. **(I)** Normalised number of synapses (defined as homer/vGlut apposition events with a maximum distance of 1 µm) per

100 µm primary dendrite. **(J)** Relative number of homer puncta apposed within 1 µm by vGlut. N = 3 biological repeats, n = at least 15 analysed neurons per condition. Scale bars, (A) 50 µm; (B-F) 5 µm. One-way ANOVA with Tukey post test. *$p < 0.05$; **$p < 0.01$ ($^{u, v}$).

Figure 6. *DKK2* is *not* upregulated at the mRNA level in post-mortem brains from AD patients. (A-C) Representative confocal images depicting microglial *DKK2* expression in the human frontal cortex. *DKK2* as well as microglial *TREM2* and *P2RY12* mRNA FISH signal in conjunction with βAmyloid IHC labelling in post-mortem human frontal cortex samples from healthy control individuals **(A)**, individuals diagnosed with pathological ageing **(B)**, and individuals diagnosed with AD **(C)**. Boxed ROIs highlight microglia expressing *DKK2* ($DAPI^+$/$DKK2^+$/$TREM2^+$/$P2RY12^+$); yellow boxed ROIs were enlarged for improved visualisation. **(D)** Quantification of microglia ($DAPI^+$/$TREM2^+$/$P2RY12^+$) numbers per maximum projected FOV (FOV = 1.8 x 10^{-2} mm^2). **(E)** Normalised *DKK2* mRNA FISH signal area per $DAPI^+$/$TREM2^+$/$P2RY12^+$ microglial cell. **(F-H)** Distribution of $DAPI^+$/$TREM2^+$/$P2RY12^+$ microglia ($Dkk2^+$, $Dkk2^-$ or total microglia (MG) populations) distances to nearest βAmyloid plaque dense core in post-mortem human frontal cortex samples. Individual plots show relative frequency distributions in individuals classified as healthy control **(F)**, pathological ageing **(G)**, and AD **(H)**. Healthy control individuals: N = 5 individuals, n = 8 fields of view); AD (Braak & Braak stage 5-6): N = 6 individuals, n = 8 fields of view; pathological ageing (Braak & Braak stage 3-4): N = 2 individuals, n = 8 fields of view. Data points represent the average of 4 FOVs analysed for each individual subject (mean ± SD); individual subject mean values were further averaged for each group of interest and summarised as mean ± SD (blue horizontal bars, red error bars). One-way ANOVA with Tukey post test ($^{w, x}$). No statistical differences identified. Scale bars, (A-C) 25 µm; (A-C enlarged ROIs) 5 µm. See also Figure 6-1, Tables 6-1 and 6-2.

Figure 1-1. Microglial *Dkk2* upregulation in $APP^{NL\text{-}G\text{-}F}$ mice – % $Dkk2^{+}$ microglia**.**

Related to Figure 1.

Relative contribution (%) of $Dkk2^{+}$ microglia versus the total microglia population in the motor cortex **(A)** and CA1 hippocampus **(B)** of $APP^{NL\text{-}G\text{-}F}$ mice as assessed by *Dkk2* mRNA FISH as well as microglial Iba1 IHC labelling. Individual data points represent the average of 4 FOVs analysed for each animal. N = 4 animals per condition and time point, n = 4 different fields of view / animal and brain region. Two-way ANOVA with Multiple comparisons test. *p < 0.05; **p < 0.01; ***p < 0.001; ****p < 0.0001 ($^{g\text{-}h}$).

Figure 2-1. Microglial *Dkk2* upregulation in *APP/PS1* mice – % *Dkk2*$^{+}$ microglia**.**

Related to Figure 2.

Relative contribution (%) of *Dkk2*$^{+}$ microglia versus the total microglia population in the motor cortex **(A)** and CA1 hippocampus **(B)** of *APP/PS1* mice as assessed by *Dkk2* mRNA FISH as well as microglial Iba1 IHC labelling. Individual data points represent the average of 4 FOVs analysed for each animal. N = 6 animals (3x females, 3x males) per time point and condition, n = 4 different fields of view / animal and brain region. Two-way ANOVA with Multiple comparisons test. *p < 0.05; **p < 0.01; ***p < 0.001; ****p < 0.0001 (^{l,m}).

Figure 3-1. Statistical analysis for microglial clustering around βAmyloid plaques.

Related to Figure 3.

(A-H) Skewness and kurtosis analysis of histograms from microglia-βAmyloid plaque nearest neighbour analysis on *APP*$^{NL\text{-}G\text{-}F}$ mice in Figure 3 in the cortex **(A-D)** and CA1 hippocampus **(E-H)** as well as at 7 months **(A,B,E,F)** and at 24 months **(C,D,G,H)**. **(I-T)** Skewness and kurtosis analysis of histograms from microglia-βAmyloid plaque nearest neighbour analysis on *APP/PS1* mice in Figure 3 in the cortex **(I-N)** and CA1 hippocampus **(O-T)** as well as at 3 months **(I,J,O,P)** 8 months **(K,L,Q,R)** and at 12 months **(M,N,S,T)**. Data points represent mean

values for individual analysed animals. *APP*$^{NL\text{-}G\text{-}F}$/control: N = 4 animals per condition and time point, n = 4 different fields of view / animal and brain region; *APP/PS1*/control: N = 6 animals (3x females, 3x males) per time point and condition, n = 4 different fields of view / animal and brain region. One-way ANOVA with Tukey post test. *p < 0.05; **p < 0.01; ***p < 0.001; ****p < 0.0001 ($^{n\text{-}p}$).

Figure 4-1. Microglial *Dkk2* upregulation in *SOD1^{G93A}* ALS mice – % *Dkk2*$^{+}$ microglia**.**

Related to Figure 4.

Relative contribution (%) of *Dkk2*$^{+}$ microglia versus the total microglia population in the L5 ventral horn spinal cord of *SOD1^{G93A}* ALS mice as assessed by *Dkk2* mRNA FISH as well as microglial Iba1 IHC labelling. Individual data points represent the average of 4 FOVs analysed for each animal. N = 3 animals per time point and condition, n = 4 fields of view per animal. Two-way ANOVA with Multiple comparisons test. *p < 0.05; **p < 0.01; ***p < 0.001; ****p < 0.0001 (^{t}).

Figure 6-1. *DKK2, TREM2,* and *P2RY12* expression the mRNA level in human post-mortem brains.

Related to Figure 6.

(A) Relative contribution (%) of *DKK2*$^{+}$ microglia versus the total microglia population in the human post-mortem frontal cortex of control, pathological ageing, and AD individuals as assessed by *DKK2, TREM2,* and *P2RY12* mRNA FISH. Normalised *TREM2* **(B)** and P2RY12 **(C)** mRNA FISH signal area per DAPI^{+}/*TREM2*$^{+}$/*P2RY12*$^{+}$ microglial cell in presence or absence of *DKK2* expression. Healthy control individuals: N = 5 individuals, n = 8 fields of view); AD (Braak & Braak stage 5-6): N = 6 individuals, n = 8 fields of view; pathological ageing (Braak & Braak stage 3-4): N = 2 individuals, n = 8 fields of view. Data points represent the average of 8 FOVs analysed for each individual subject (mean ± SD for **(A)**, mean for **(B,C)**); individual subject mean values were further averaged for each group of interest and summarised as mean ± SD (blue horizontal bars, red error bars). One-way ANOVA with Tukey post test ($^{y, z, ab}$). No statistical differences identified.

1271 **Table 1 Statistical table**

Table 6-1. Human sample demographic data.

Related to Figure 6.

Table listing demographic data of individual subjects contributing to the generation of data set in Figure 6. Clinical presentation as well as post-mortem brain assessments are shown (brain weight, post-mortem (PM) delay, Braak & Braak stage, CERAD score, THAL stage, and ABC score).

Table 6-2. mRNA FISH signal detection parameters.

Related to Materials and methods, as well as Figure 6.

Signal detection parameters used to identify *DKK2*, *TREM2*, and *P2RY12* mRNA FISH signal on confocal images form human samples using HALO software with the FISH-IF v2.0.4 module (Indica Labs).

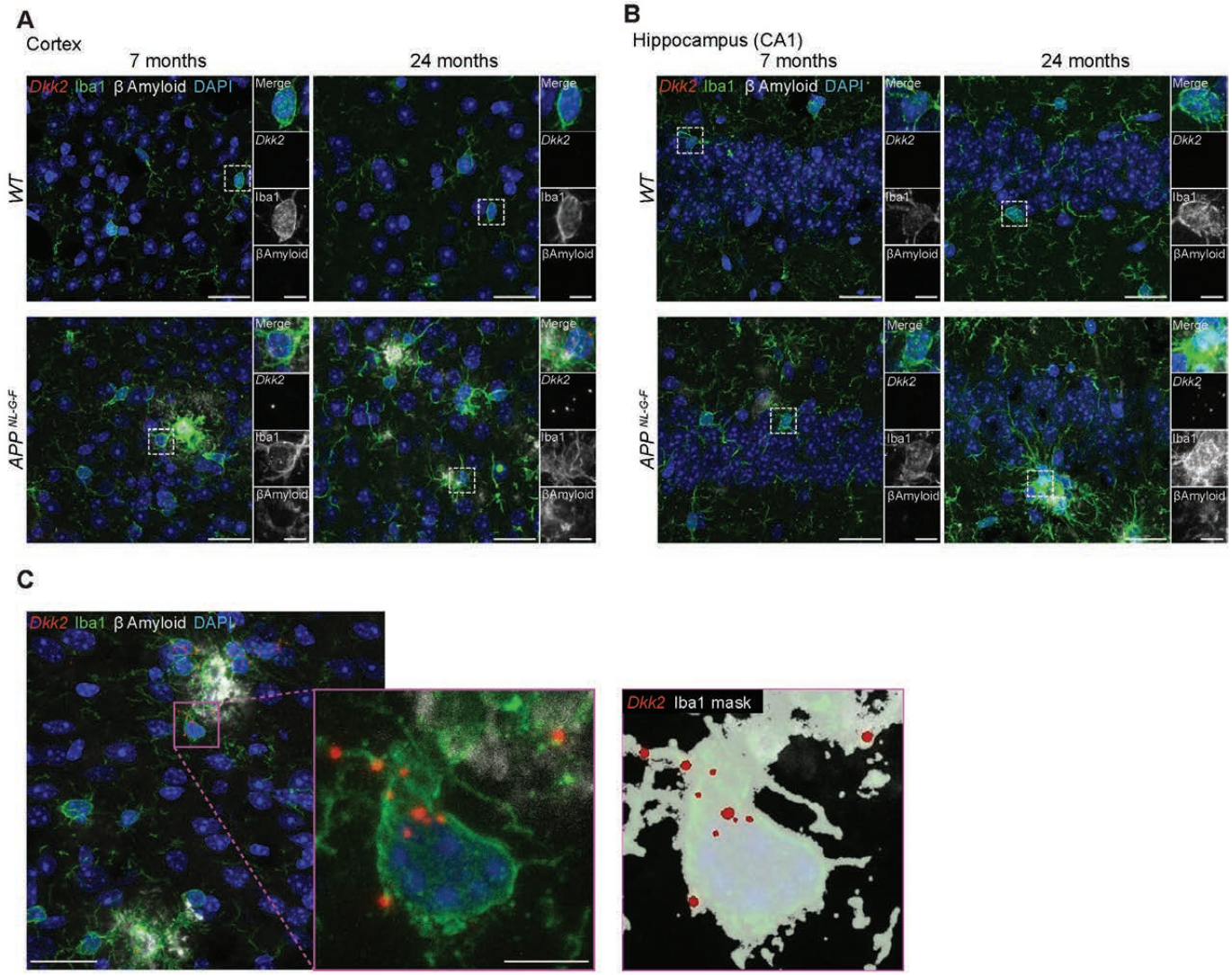

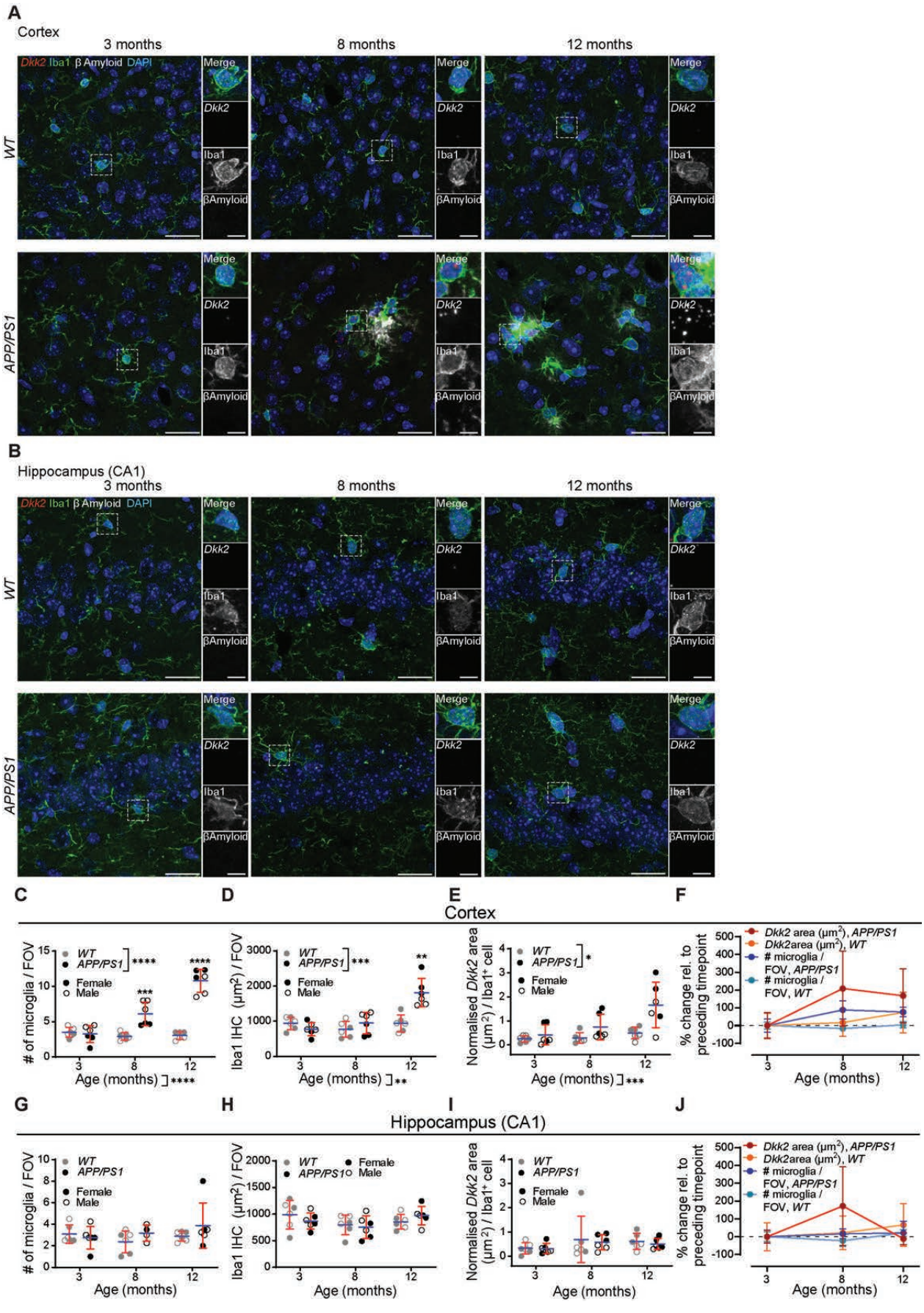

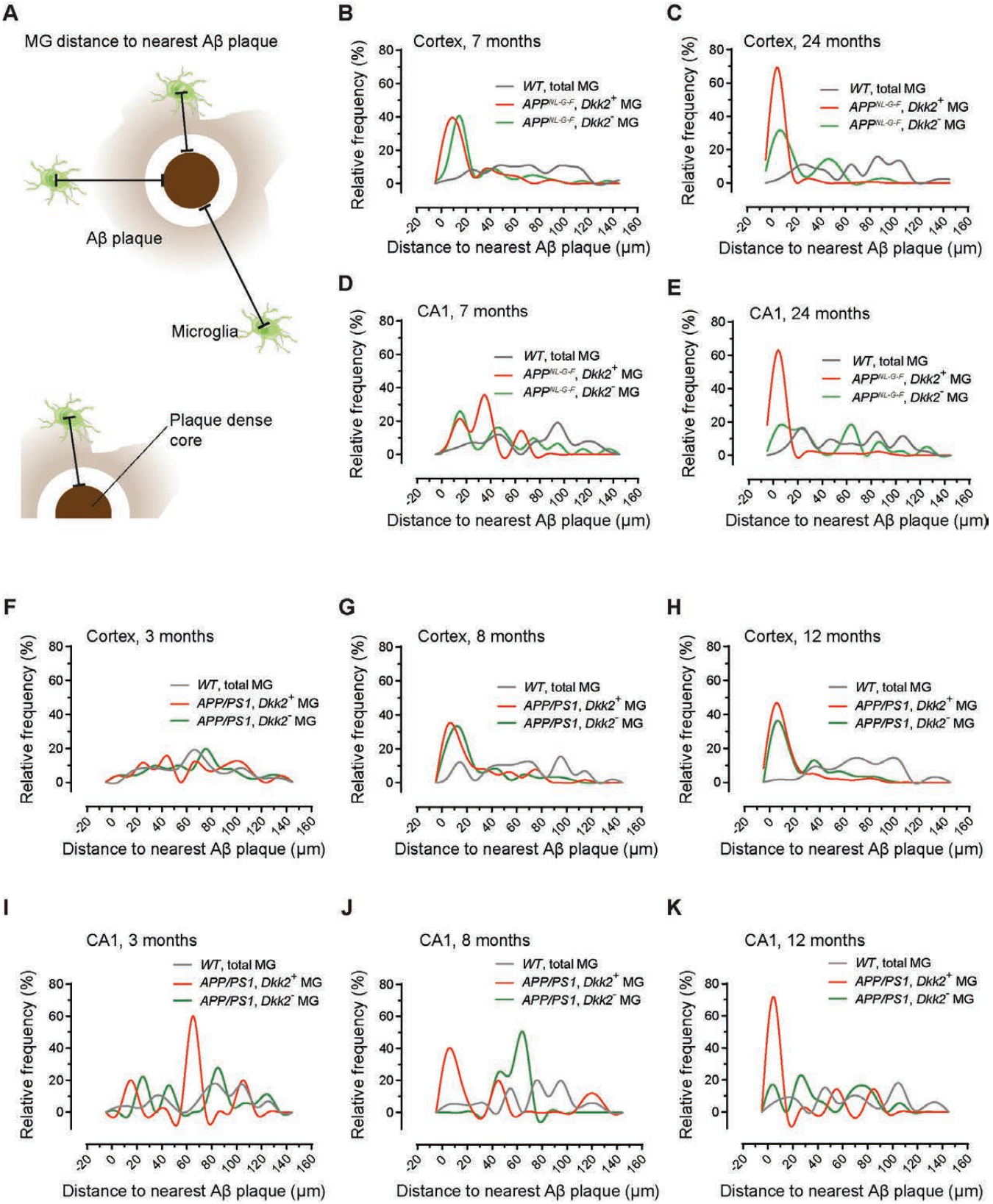

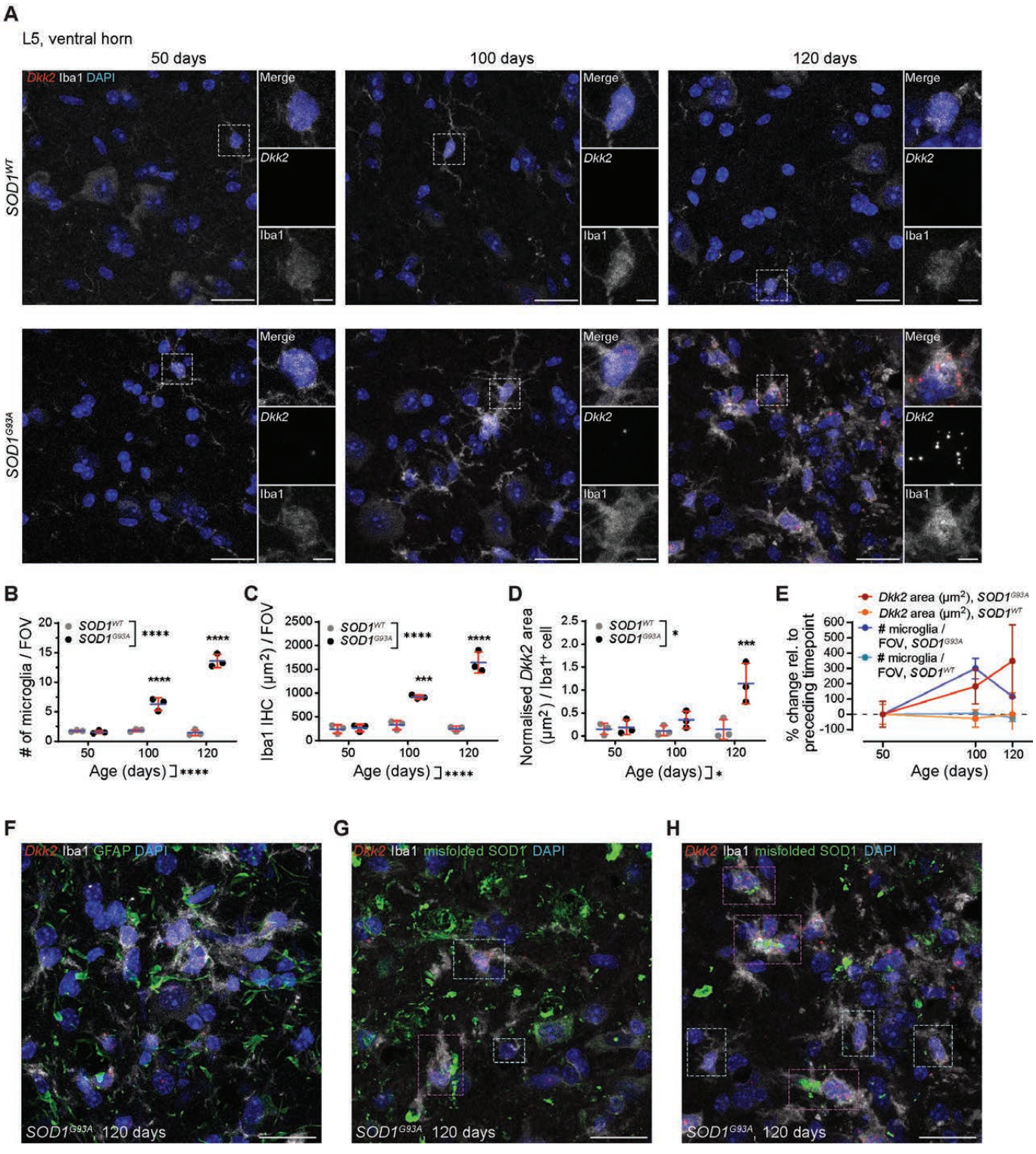

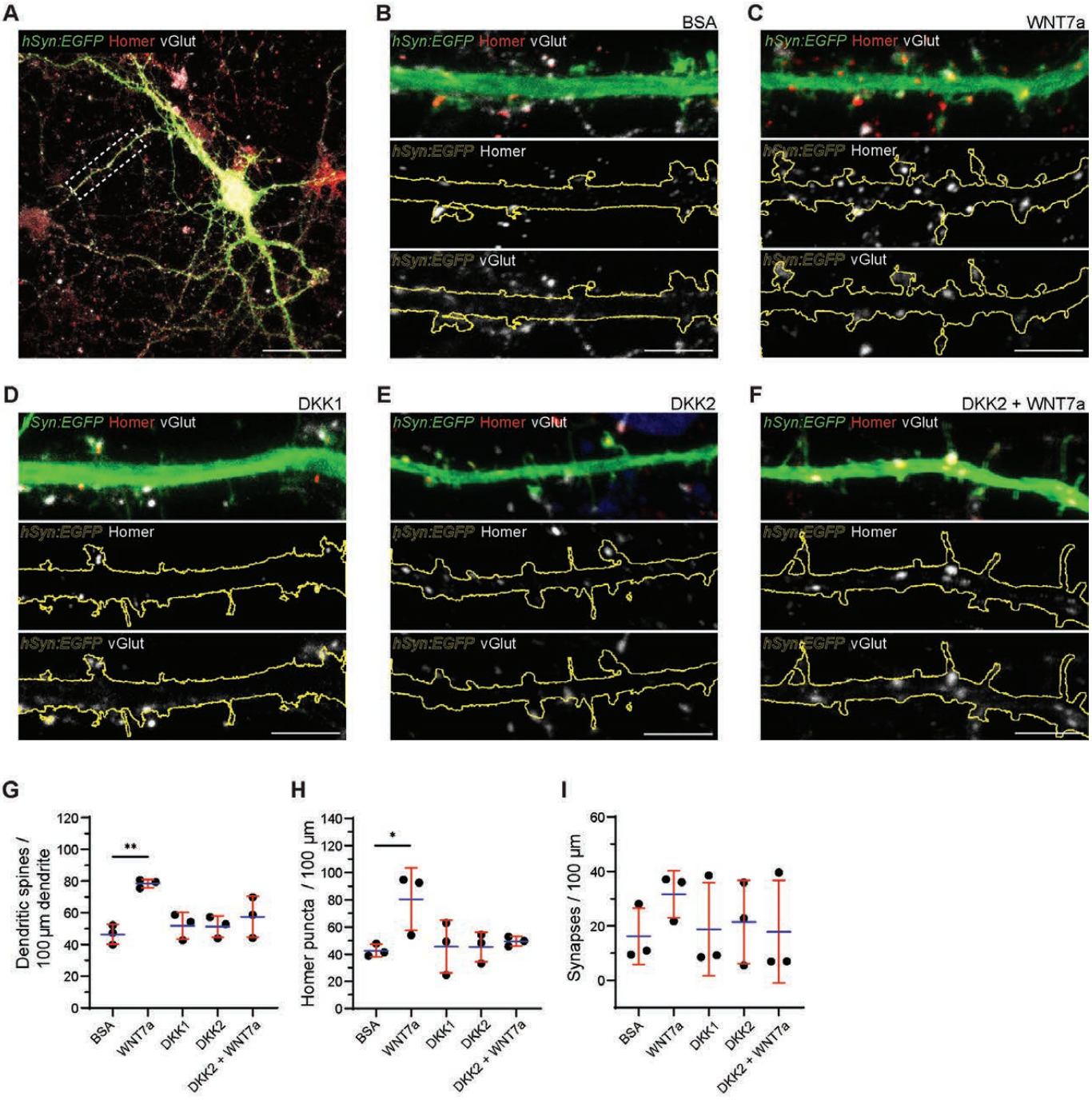

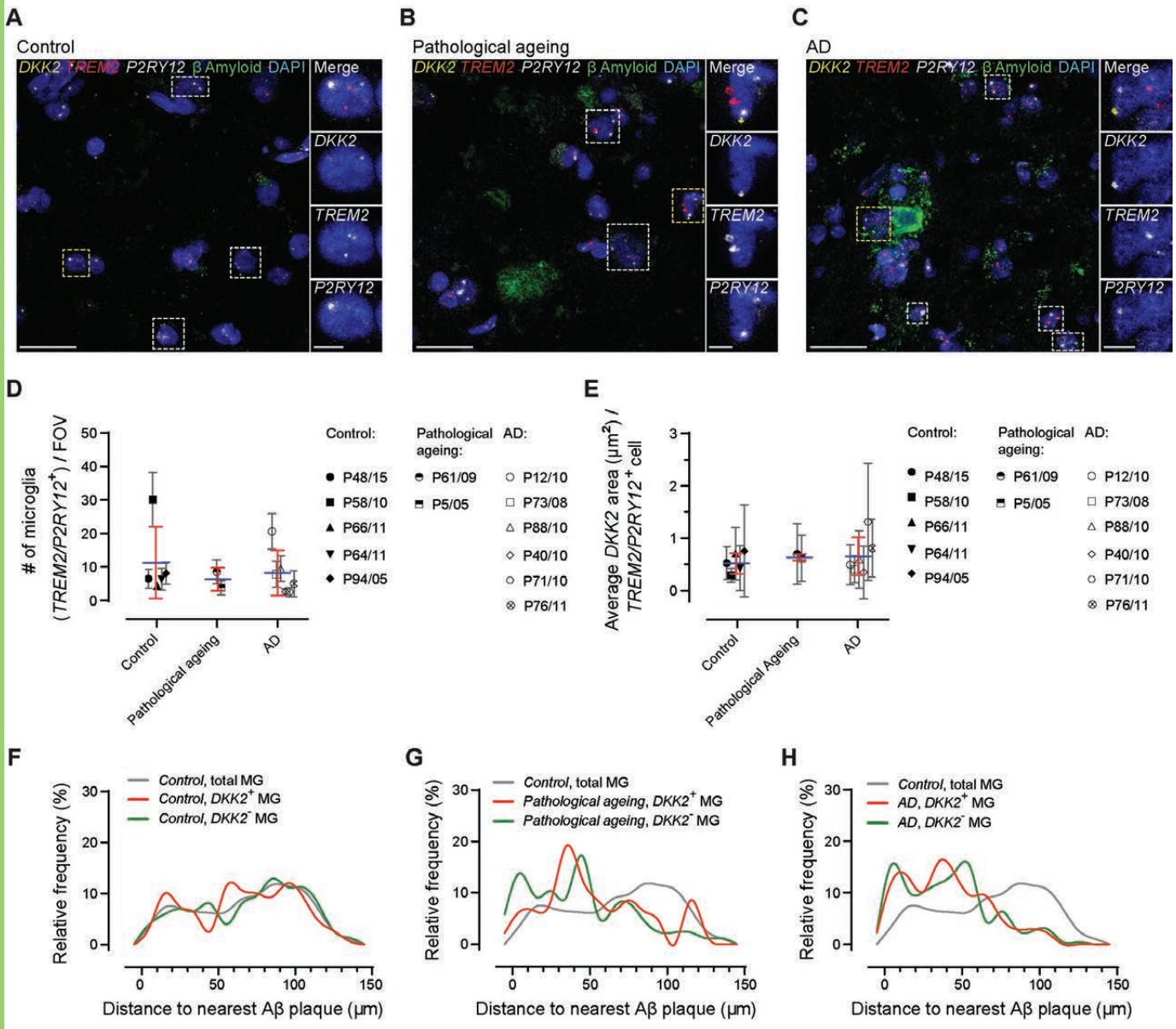

	Data Structure	Type of test
a	Normal distribution	Two-Way ANOVA with Šidák multiple comparisons test
b	Normal distribution	Two-Way ANOVA with Šidák multiple comparisons test
c	Normal distribution	Two-Way ANOVA with Šidák multiple comparisons test
d	Normal distribution	Mixed-effects analysis with Šidák multiple comparisons test
e	Normal distribution	Two-Way ANOVA with Šidák multiple comparisons test
f	Normal distribution	Two-Way ANOVA with Šidák multiple comparisons test
g	Normal distribution	Two-Way ANOVA with Šidák multiple comparisons test
h	Normal distribution	Two-Way ANOVA with Šidák multiple comparisons test
i	Normal distribution	Two-Way ANOVA with Šidák multiple comparisons test
j	Normal distribution	Two-Way ANOVA with Šidák multiple comparisons test
k	Normal distribution	Two-Way ANOVA with Šidák multiple comparisons test
l	Normal distribution	Two-Way ANOVA with Šidák multiple comparisons test
m	Normal distribution	Two-Way ANOVA with Šidák multiple comparisons test
n	Normal distribution	One-Way ANOVA with Tukey's multiple comparison test
o	Normal distribution	One-Way ANOVA with Tukey's multiple comparison test
p	Normal distribution	One-Way ANOVA with Tukey's multiple comparison test
q	Normal distribution	Two-Way ANOVA with Šidák multiple comparisons test
r	Normal distribution	Two-Way ANOVA with Šidák multiple comparisons test
s	Normal distribution	Two-Way ANOVA with Šidák multiple comparisons test
t	Normal distribution	Two-Way ANOVA with Šidák multiple comparisons test
u	Normal distribution	One-Way ANOVA with Tukey's multiple comparison test
v	Normal distribution	One-Way ANOVA with Tukey's multiple comparison test
w	Normal distribution	One-Way ANOVA with Tukey's multiple comparison test
x	Normal distribution	One-Way ANOVA with Tukey's multiple comparison test
y	Normal distribution	One-Way ANOVA with Tukey's multiple comparison test
z	Normal distribution	One-Way ANOVA with Tukey's multiple comparison test
ab	Normal distribution	One-Way ANOVA with Tukey's multiple comparison test

Power
p = 0.0101 (tp), p = 0.0002 (gt)
p = 0.1821 (tp), p = 0.0018 (gt)
p = 0.0245 (tp), p = 0.0013 (gt)
p = 0.0005 (tp), p = 0.0051 (gt)
p = 0.0119 (tp), p = 0.0288 (gt)
p = 0.1363 (tp), p = 0.0652 (gt)
p = 0.0240 (tp), p = 0.0004 (gt)
p = 0.0784 (tp), p = 0.0093 (gt)
p < 0.0001 (tp), p < 0.0001 (gt)
p = 0.0030 (tp), p = 0.0006 (gt)
p = 0.0003 (tp), p = 0.0391 (gt)
p = 0.3563 (tp), p = 0.7931 (gt)
p = 0.1691 (tp), p = 0.7041 (gt)
various
various
various
p < 0.0001 (tp), p = 0.0001 (gt)
p < 0.0001 (tp), p = 0.0001 (gt)
p = 0.0154 (tp), p = 0.0193 (gt)
p = 0.9125 (tp), p = 0.0073 (gt)
p = 0.0023
p = 0.0309
p = 0.4507
p = 0.7689
p = 0.8650
p = 0.2349
p = 0.1056